HAL open science

Complex geochronological record of an emblematic Variscan eclogite (Haut-Allier, French Massif Central)

Luc de Hoÿm de Marien, Pavel Pitra, Marc Poujol, Nathan Cogné, Florence Cagnard, Benjamin Le Bayon

To cite this version:

Luc de Hoÿm de Marien, Pavel Pitra, Marc Poujol, Nathan Cogné, Florence Cagnard, et al.. Complex geochronological record of an emblematic Variscan eclogite (Haut-Allier, French Massif Central). Journal of Metamorphic Geology, 2023, 41 (7), pp.967-995. 10.1111/jmg.12733 . insu-04101059v2

HAL Id: insu-04101059

https://insu.hal.science/insu-04101059v2

Submitted on 5 Jun 2023

HAL is a multi-disciplinary open access archive for the deposit and dissemination of scientific research documents, whether they are published or not. The documents may come from teaching and research institutions in France or abroad, or from public or private research centers.

L'archive ouverte pluridisciplinaire **HAL**, est destinée au dépôt et à la diffusion de documents scientifiques de niveau recherche, publiés ou non, émanant des établissements d'enseignement et de recherche français ou étrangers, des laboratoires publics ou privés.

Distributed under a Creative Commons Attribution - NonCommercial - NoDerivatives 4.0 International License

Check for updates

Received: 21 June 2022 | Revised: 3 April 2023 | Accepted: 8 April 2023

DOI: 10.1111/jmg.12733

ORIGINAL ARTICLE

Journal of METAMORPHIC GEOLOGY WILEY

Complex geochronological record of an emblematic Variscan eclogite (Haut-Allier, French Massif Central)

Luc de Hoÿm de Marien[1,2] | **Pavel Pitra**[1,2] | **Marc Poujol**[2] | **Nathan Cogné**[2] | **Florence Cagnard**[3] | **Benjamin Le Bayon**[3]

[1]Centre for Lithospheric Research, Czech Geological Survey, Prague, Czech Republic

[2]Univ Rennes, CNRS, Géosciences Rennes - UMR 6118, Rennes, France

[3]Bureau de Recherches Géologiques et Minières – BRGM, Orléans cedex 2, France

Correspondence
Luc de Hoÿm de Marien, Centre for Lithospheric Research, Czech Geological Survey, Prague CZ-118 21, Czech Republic.
Email: luc.dehoym@gmail.com

Funding information
Czech Geological Survey grant, Grant/Award Number: 311190; French Geological Survey (BRGM)

Handling Editor: Dr. Chunjing Wei

Abstract

Two eclogite samples from the Haut-Allier record a prograde evolution from ~20 kbar, 650°C to 750°C, 22–23 kbar followed by heating up to 850–875°C and partial melting. Incipient decompression in high-pressure granulite facies conditions (19.5 kbar, 875°C) was followed by exhumation to high-temperature amphibolite facies conditions (<9 kbar, 750–850°C). Following a detailed geochemical, petrological, and geochronological investigation using trace-element data and laser ablation inductively coupled plasma mass spectrometry U–Pb dating of zircon, apatite, and rutile, the eclogites reveal an Ordovician (c. 490 Ma) rifting event followed by Devonian (c. 370–360 Ma) subduction and Carboniferous (c. 350 Ma) exhumation in this part of the French Massif Central. The previously proposed Silurian age for the subduction, which strongly influenced many tectonic models, is definitively rejected. In the light of other geological data from the French Massif Central, including the lithological and geochemical zoning of calc-alkaline Devonian volcanism, we propose a southward polarity of the subduction and question the very existence of the so-called Massif Central Ocean. Furthermore, we infer that following subduction, the eclogites were relaminated to the upper plate and exhumed at the rear of the magmatic arc pointing to similarities with the geodynamics of the Bohemian Massif.

The petrochronological record of zircon is particularly complex. Metamorphic zircon with clear eclogitic rare-earth elements patterns (no Eu anomaly and flat heavy rare-earth elements) and inclusions (garnet, rutile, and omphacite) shows concordant apparent ages that spread from c. 380 down to c. 310 Ma. This apparent age pattern strongly contrasts with the well-defined age of apatite and rutile of c. 350 Ma. Apparent zircon ages younger than 350 Ma unequivocally testify that zircon can recrystallize outside the conditions of the eclogite facies, which resets the U–Pb while preserving an apparent eclogitic signature. Local fractures filled by analcite, thomsonite, plagioclase, and biotite testify to late interaction of the eclogites with alkaline fluids at relatively low temperatures. This interaction, possibly at c. 310 Ma or later, could lead to the recrystallization of zircon while leaving apatite unaffected.

This is an open access article under the terms of the Creative Commons Attribution-NonCommercial-NoDerivs License, which permits use and distribution in any medium, provided the original work is properly cited, the use is non-commercial and no modifications or adaptations are made.
© 2023 The Authors. *Journal of Metamorphic Geology* published by John Wiley & Sons Ltd.

KEYWORDS
apatite, eclogite, petrochronology, Variscan belt, zircon

1 | INTRODUCTION

Eclogites in ancient orogens are commonly interpreted as the result of past subduction prior to continental collision (Ernst & Liou, 2008; Godard, 2001; Miyashiro, 1961, 1972). Although eclogites may occasionally form during continental collision, dating eclogite facies metamorphism commonly provides the best approximation of the onset of convergence, which has critical implications for the formulation of tectonic scenarios.

The French Massif Central (FMC) is one the Western European Palaeozoic massifs and belongs to the high-grade core of the Variscan orogen (e.g., Matte, 1986; Lardeaux et al., 2014; Martínez Catalán et al., 2021; Figure 1a) that resulted from the convergence between Laurussia and Gondwana. During this convergence, terranes previously rifted from the Gondwana margin during the opening of Ordovician oceanic domains (Nance & Linnemann, 2008; von Raumer & Stampfli, 2008) were amalgamated back to Gondwana (Kroner & Romer, 2013; Matte, 1986; Stampfli et al., 2013). This event is recorded in the Massif Central by high-grade metamorphism including eclogite facies metamorphism (e.g., Matte, 1991) that developed in terrains from the thinned Gondwanan continental margin (Lardeaux, 2014). The FMC consequently bears strong similarities with the other massifs of the European Variscan belt (e.g., Lardeaux et al., 2014; Martínez Catalán et al., 2021; Matte, 1986). However, the necessary correlations at the scale of the orogen are hampered by the lack of modern geochronological data in the FMC. There, only a limited number of studies focused on the geochronology of the eclogites. These studies often adopted different methodologies and proposed different ages for the eclogite facies metamorphism.

Several studies proposed a Silurian age for the subduction event in the FMC (Ducrot et al., 1983; Paquette et al., 1995; Pin & Lancelot, 1982). This age was inferred principally from U–Pb results obtained by dissolution of a zircon population. A more recent similar Silurian age obtained by U–Pb laser ablation inductively coupled plasma mass spectrometry (LA-ICP-MS) dating on zircon has been attributed to the eclogite facies event only by analogy with the results from the three aforementioned studies (Berger et al., 2010). However, two other recent studies, carried out using a multimineral and multichronometer approach and based on a well-constrained petrological framework, rather suggest subduction during the Devonian in the southern part of the FMC (Lotout et al., 2018, 2020). Furthermore, although recent studies have argued that the Silurian ages should be abandoned in the whole FMC given their technical limitations and the complexity of the geochronological record of the rocks (Benmammar et al., 2020; Lotout et al., 2018, 2020; Paquette et al., 2017), both ages (i.e., Silurian and Devonian) are still used in the literature (e.g., Martínez Catalán et al., 2021; Vanderhaeghe et al., 2020). Taking the Silurian ages and their regional distribution into account (Figure 1) suggests a southward younging of the eclogite facies metamorphism and a very long-lasting subduction event (430 to 360 Ma; Figure 1b), with important consequences for the tectonic models and correlation of the FMC with other European Variscan massifs. A reassessment of the eclogite outcrops from which this Silurian age is derived is therefore essential.

This contribution presents geochronological results obtained in two eclogite samples and one closely associated felsic diatexite (Supporting Information S1) from a locality where a previous study suggested a Silurian age for the eclogite facies metamorphism. U–Pb isotopes of zircon, apatite, and rutile separated from the eclogites are studied in situ using LA-ICP-MS. The isotopic results are interpreted in the framework of an already published petrological study (de Hoÿm de Marien et al., 2020) complemented by new petrographic data and the determination of microinclusions in zircon by Raman spectroscopy, together with trace-element data in zircon and rutile.

2 | GEOLOGICAL BACKGROUND

The FMC is interpreted as a Palaeozoic nappe stack intruded by syn- to post-orogenic granitoids, dissected by late-orogenic migmatitic domes, and unconformably overlain by Upper Carboniferous sediments (e.g., Faure et al., 2009; Lardeaux, 2014). The nappe stack involves several units established from lithological association and tectonometamorphic consideration (Ledru et al., 1989). The studied area belongs to the eastern part of the FMC where the following succession of units is generally recognized from north to south (Figure 1b).

The northernmost *Morvan and Brévenne units* consist of low-grade Devonian volcano-sedimentary series respectively interpreted as arc and back-arc series (e.g., Delfour, 1989; Leloix et al., 1999). In the northerly Morvan area, the series include fossiliferous carbonates of the upper Devonian and andesites (Figure 1b). In the southerly Brévenne area, the volcanic rocks belong to a

15251314, 0, Downloaded from https://onlinelibrary.wiley.com/doi/10.1111/jmg.12733 by Cochrane France, Wiley Online Library on [03/06/2023]. See the Terms and Conditions (https://onlinelibrary.wiley.com/terms-and-conditions) on Wiley Online Library for rules of use; OA articles are governed by the applicable Creative Commons License

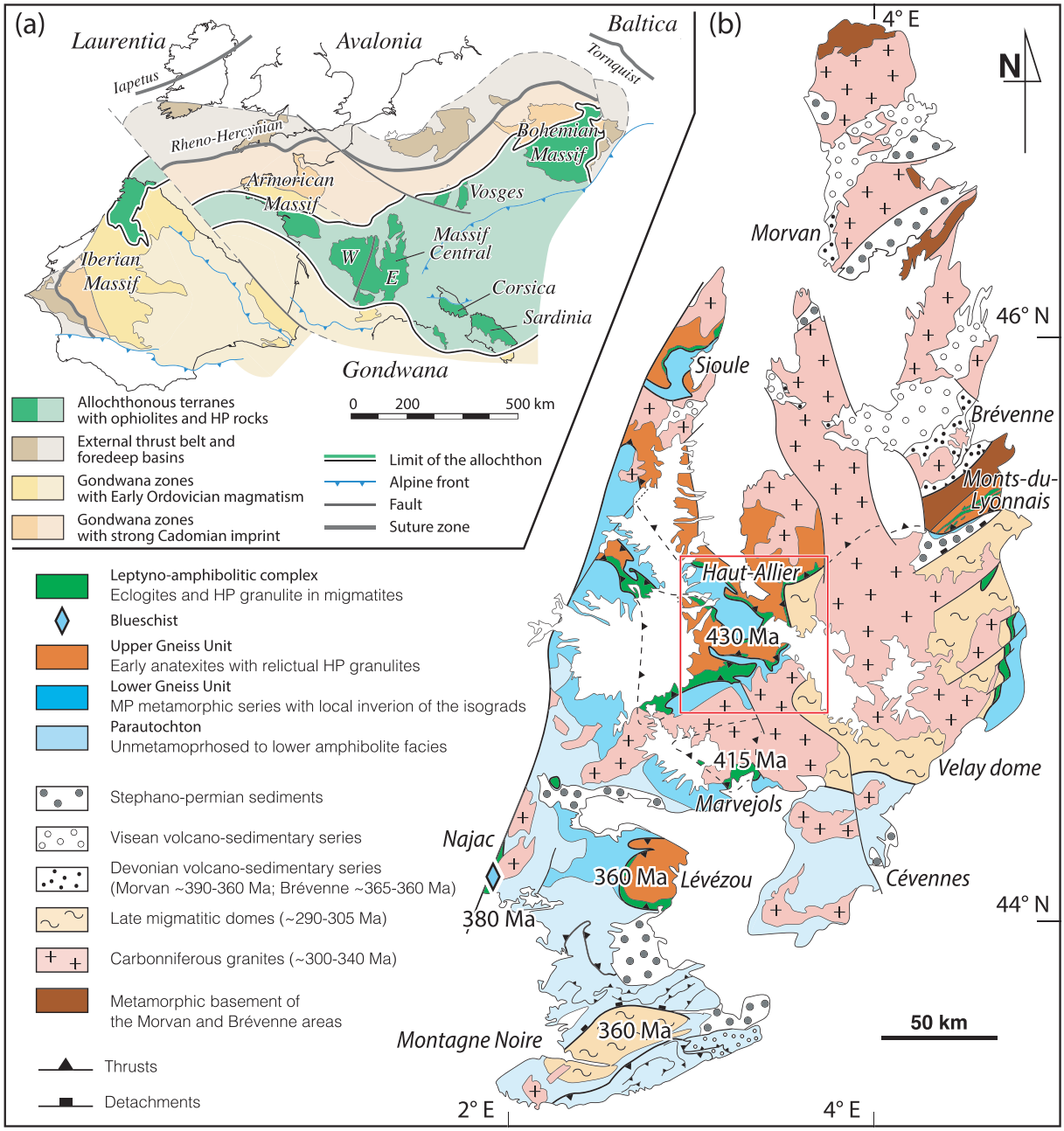

FIGURE 1 (a) Sketch of the main Variscan massifs and terranes of the European Variscan orogen (modified after Martínez Catalán et al., 2007, 2021) with the position of the French Massif Central (E and W denote its eastern and western parts, respectively). (b) Simplified tectonic map of the eastern part of the French Massif Central (modified after Ledru et al., 1989). The ages interpreted as the age of the eclogite-facies metamorphism are reported (see main text for references). Ages for the Devonian and Carboniferous magmatism are also reported in the text. Age of the emplacement of the late migmatite domes is after Barbey et al. (2015), Roger et al. (2015), and Poujol et al. (2016). The red rectangle shows the area covered by Figure 2. [Colour figure can be viewed at wileyonlinelibrary.com]

typical bimodal spilite–keratophyre association including pillow lavas indicating the marine character of the series (Peterlongo, 1958, 1970). The rocks are of Famennian age (c. 360 Ma) and have been interpreted as a suprasubductional complex emplaced in a settings involving incipient rifting of a volcanic arc built upon a thin continental crust (Pin & Paquette, 1997). The regional lithological zoning of the volcanic rocks and the associated southward decreasing enrichment in incompatible elements suggest that the Devonian subduction was dipping to the south (Pin et al., 1982; Pin & Paquette, 2002). The metamorphic basement of the Morvan and Brévenne areas includes (undated) eclogites (Godard, 1990) and is attributed to the Upper Gneiss Unit (UGU; e.g., Faure et al., 1997; Leloix et al., 1999). This is however open to discussion, and this basement is set apart in Figure 1b.

15251314, 0, Downloaded from https://onlinelibrary.wiley.com/doi/10.1111/jmg.12733 by Cochrane France, Wiley Online Library on [03/06/2023]. See the Terms and Conditions (https://onlinelibrary.wiley.com/terms-and-conditions) on Wiley Online Library for rules of use; OA articles are governed by the applicable Creative Commons License

The UGU consists of paragneisses and orthogneisses, as well as metamorphosed basic and ultrabasic rocks. The metasediments were deposited during the Ediacaran (Chelle-Michou et al., 2017). The base of the UGU is composed of a bimodal igneous association referred to as the Leptyno-Amphibolitic Complex (LAC; Forestier, 1961, Santallier et al., 1988) typically considered to record a Cambro–Ordovician rifting event (e.g., Lotout et al., 2017; Pin & Lancelot, 1982; Pin & Marini, 1993). The mafic rocks, locally associated with garnet peridotites (e.g., Gardien et al., 1988, 1990; Lasnier, 1968, 1971), are metamorphosed in the eclogite facies at high temperature (e.g., Lardeaux et al., 2001; Mercier et al., 1989; Nicollet, 1977; Nicollet & Leyreloup, 1978). The eclogite facies is interpreted in terms of subduction of the so-called Massif-Central Ocean (e.g., Matte, 1986), and consequently, the LAC is considered as a suture zone (e.g., Matte & Burg, 1981). As mentioned in Section 1, the dating of the subduction event is controversial with inferred ages between 420 and 360 Ma. The subsequent decompression of the LAC is recorded by a granulitic overprint in various lithologies (e.g., Burg & Leyreloup, 1989; Forestier et al., 1973; Lasnier, 1968, 1977; Marchand, 1974; Mercier et al., 1991) and tentatively dated at c. 360 Ma (Schulz, 2014). Further decompression is associated with the emplacement of granitoids at c. 315 Ma (Gardien et al., 2011; Laurent et al., 2017), and final cooling is constrained between 300 and 275 Ma (Gardien et al., 2011).

A *Middle Allochthon Unit*, so far only reported in the Najac area (Figure 1b), is tentatively recognized by comparison with the neighbouring Limousin and Armorican domains (Benmammar et al., 2020), but its extension in the Eastern FMC is unclear. It contains relicts of eclogites dated at c. 380 Ma (Lu–Hf in garnet and U–Pb in zircon; Lotout et al., 2018).

The *Lower Gneiss Unit* is composed of paragneisses and orthogneisses with varied metamorphic overprint. The paragneisses of probable Ediacaran protolith (Couzinié et al., 2019; Figure 1b), like those of the UGU, record a Cadomian orogenic event prior to the Variscan orogeny (Couzinié et al., 2017). Paragneisses south of Marvejols (Figure 1b) display an inverted medium-pressure metamorphic zoning attributed to the underthrusting below the UGU during the Variscan orogeny (Burg et al., 1984).

The *Parautochton* is mostly composed of metapelites that display a limited metamorphic imprint ranging from greenschist to low-amphibolite grade (e.g., Faure et al., 1999).

The entire eastern FMC is intruded by abundant Carboniferous granitoids (Figure 1b), including mantle-derived Mg–K-rich (monzo)diorites and lamprophyres ("vaugnerites"), resulting from polyphase melting from c. 340 to c. 300 Ma (e.g., Barbey et al., 2015; Couzinié et al., 2014; Gardien et al., 2011; Laurent et al., 2017; Moyen et al., 2017).

The studied eclogites were sampled in the Haut-Allier (Figure 2), where the eclogite-bearing UGU is inferred to thrust over the Lower Gneiss Unit (LGU), devoid of HP metamorphism (e.g., Burg et al., 1984). The metabasic rocks of the LAC have geochemical affinities with ocean-floor tholeiites or back-arc basalts (Giraud et al., 1984). The close association with continental crustal rocks points to a thinned continental margin setting (e.g., Lardeaux, 2014). The protoliths are not dated. The dominant metamorphic grade ranges from the amphibolite to the granulite facies, but eclogite lenses are also present (Lasnier, 1977). Ultramafic rocks include garnet-bearing peridotites (Lasnier, 1968), but available *P–T* conditions from a garnet–pyroxene granulite indicate 20 kbar, 800°C (Pin & Vielzeuf, 1988). Similar conditions (~800–900°C at 18 kbar) are recorded in a coronitic gabbro, followed by an LP–HT overprint at ~4 kbar, 650°C (Nicollet et al., 1993).

The age of the HP metamorphism was estimated in the pioneering study of Ducrot et al. (1983) at 430 ± 20 Ma by U–Pb dating of a dissolved population of zircon from an eclogite found at the locality of La Borie (Figure 2). Because of the importance of the age of the HP metamorphic stage in the eclogites and the problematic reliability, discussed above, of the method employed by Ducrot et al., the age of the eclogite facies metamorphism of the La Borie eclogite is re-evaluated in this paper. The eclogites occur within a variably retrogressed hectometre lens embedded in a sillimanite-bearing diatexite in close association with a felsic orthogneiss. The eclogites underwent prograde metamorphism in the eclogite facies from 650°C at 20 kbar to 750°C at 22–23 kbar and crossed the solidus during an isobaric temperature increase up to 850–875°C (de Hoÿm de Marien et al., 2020). Following incipient decompression to ~19 kbar in the HP granulite facies, further decompression to 5–10 kbar at 750–850°C led to partial recrystallization in the HT amphibolite facies.

3 | METHODS

3.1 | Geochemistry

Samples for whole-rock chemistry were cleaned from weathering alteration, successively crushed in a jaw and a roller crusher, and reduced in powder with a planetary crusher in an agate bowl. Powders were analysed at the Geochemical and Petrographical Research Center in

15251314, 0, Downloaded from https://onlinelibrary.wiley.com/doi/10.1111/jmg.12733 by Cochrane France, Wiley Online Library on [03/06/2023]. See the Terms and Conditions (https://onlinelibrary.wiley.com/terms-and-conditions) on Wiley Online Library for rules of use; OA articles are governed by the applicable Creative Commons License

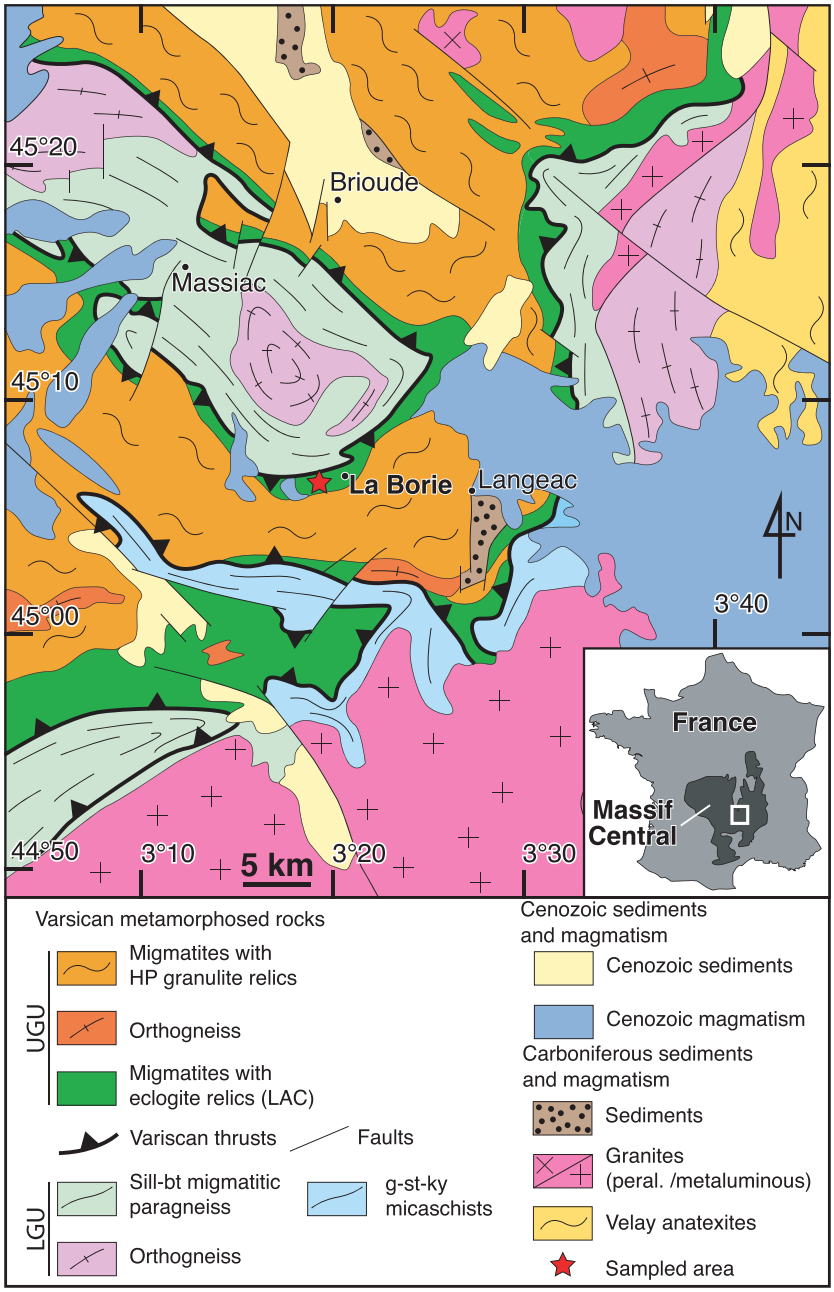

FIGURE 2 Geological map of the study area and its location in the French Massif Central (white rectangle in the inset). The samples have been gathered west of La Borie (45°6′45.29″N; 3°19′55.83″E; WGS84) in the LAC. LAC, Leptyno-Amphibolitic Complex; LGU, Lower Gneiss Unit; UGU, Upper Gneiss Unit. [Colour figure can be viewed at wileyonlinelibrary.com]

Nancy, France (SARM laboratory, CNRS-CRPG), for major and trace elements using Inductively Coupled Plasma Optical Emission Spectrometry and Mass Spectrometry (ICP-MS) respectively. FeO (vs. Fe_2O_3) was analysed by wet titration. Whole-rock geochemical data are accessible in Supporting Information S2.

3.2 | U–Pb trace-elements petrochronology

A mineral separation procedure has been applied to concentrate zircon and apatite grains for U–Pb dating using the facilities available at Géosciences Rennes (University of Rennes). The samples were crushed, and only the powder fraction with a diameter <250 μm was kept. Heavy minerals were first concentrated by Wilfley table, and magnetic minerals were removed with an isodynamic Frantz separator. Non-magnetic heavy minerals were afterwards separated with heavy liquids. The concentrated zircon and apatite grains were handpicked under a binocular microscope. The selected minerals were embedded in epoxy mounts, grounded to the middle of the grain, and then polished on a lap wheel.

Separated zircon and apatite grains were imaged by cathodoluminescence (CL) using a Reliotron CL system equipped with a digital colour camera available at the GeOHeLiS analytical platform (OSUR, University of

15251314, 0, Downloaded from https://onlinelibrary.wiley.com/doi/10.1111/jmg.12733 by Cochrane France, Wiley Online Library on [03/06/2023]. See the Terms and Conditions (https://onlinelibrary.wiley.com/terms-and-conditions) on Wiley Online Library for rules of use; OA articles are governed by the applicable Creative Commons License

Rennes). Thin section imaging of zircon was performed at Clermont-Ferrand using a scanning electron microscope equipped with a CL system (JEOL JSM-6400, Laboratoire Magmas et Volcans, Clermont-Ferrand). Rutile crystals in thin section were imaged using back-scattered electrons (JEOL IT 300 LA EDS scanning electron microscope, CMEBA platform, University of Rennes).

U–Pb geochronology of zircon, rutile, and apatite grains was conducted by in situ LA-ICP-MS at the GeOHeLiS analytical platform (OSUR, University of Rennes) using an ESI NWR193UC Excimer laser coupled to an Agilent quadrupole 7700x ICP-MS equipped with a dual pumping system to enhance sensitivity (Paquette et al., 2014). The instrumental conditions are reported in Tables S1–S3, and details for each analytical sessions may be found in the first sheet of Supporting Information S3 and S4 (BR18 and BR19—eclogite samples and BR60—diatexites sample). Further information on the dating protocol can be found in Nosenzo et al. (2022) for zircon, Lotout et al. (2020) for rutile, and in Pochon et al. (2016) for apatite.

Zircon, apatite, and rutile were analysed during several analytical sessions with distinct analytical conditions (beam size, repetition rate, fluence, and analysed masses) summarized in Supporting Information S3 and S4. Data were corrected for U–Pb and Th–Pb fractionation and for the mass bias by standard bracketing with repeated measurements of the GJ-1 zircon standard (Jackson et al., 2004), Madagascar apatite standard (Thomson et al., 2018), or R10 rutile standard (Luvizotto et al., 2009). In addition, zircon, apatite, and rutile reference materials were measured along with the unknowns to monitor the accuracy of the analyses. For the sake of clarity, the ages indicated for the standard in the following text (and Tables S1–S3) were calculated using all the data (obtained during different analytical session), and the ages produced during individual analytical session are indicated in Supporting Information S3 and S4. McClure (Schoene & Bowring, 2006; 524.5 ± 4.5; $n = 13$; MSWD = 0.66) and Durango (McDowell et al., 2005; 32 ± 0.5; $n = 14$; MWSD = 1.2) apatite reference materials were measured along with the apatite analyses. Accuracy during the rutile analyses was monitored using rutile R19 (Zack et al., 2011; 484.5 ± 9; $n = 6$; MSWD = 0.1) and R632 (Axelsson et al., 2018; 500 ± 6 Ma; $n = 10$; MSWD = 1.3) reference materials. Data for Zr in rutile were corrected using the rutile R10 (Luvizotto et al., 2009), and rutile R19 (Zack et al., 2011) was measured along with the unknown as a secondary reference material.

Zircon crystal domains have various shapes and sizes (see below). In order to ensure that all the different domains were analysed without compromising the precision and accuracy of the geochronological results, different analytical procedures were implemented. First, the zircon grains were characterized for trace element and isotopic data at the same time, using a small rectangular beam size (37 * 14 μm). Data for trace elements in zircon were corrected using NIST612 glass (Kent et al., 2004), and zircon standard 91500 (Wiedenbeck et al., 1995; Wiedenbeck et al., 2004; 1080 ± 7.5 Ma; $n = 23$; MSWD = 2.5) was measured along with the unknowns as a secondary standard following the procedure described in Nosenzo et al. (2022). In a second time, large zircon crystals of known trace-element chemistry (i.e., already analysed with small-sized beam) were targeted for U–Pb isotope analysis using a larger rounded beam size (50 μm) in order to enhance analytical precision. The accuracy of the analyses was monitored using the zircon standard Plešovice (Sláma et al., 2008; 337 ± 1.3 Ma; $n = 13$; MSWD = 0.5) as a secondary reference material.

Data reduction was carried out with Iolite v4 (Paton et al., 2011). Reproducibility and age uncertainties of reference material Plešovice and 91500 were propagated by quadratic sum to the analysed zircon grains according to Horstwood et al. (2016). Concordia and lower intercept ages and diagrams were generated using IsoplotR (Vermeesch, 2018). All errors given in Supporting Information S3 and S4 are listed at two sigmas.

Raman spectroscopy was performed at the Laboratoire Magmas et Volcans (Clermont-Ferrand, France). Raman spectra were obtained using a Renishaw InVia confocal Raman microspectrometer, equipped with a 532 nm diode laser (output power of 200 mW), a Peltier-cooled CCD detector, a motorized XY stage, and a Leica DM 2500M optical microscope. Back-scattered geometry allowed to collect the scattered light and a dielectric edge filter to reject reflected laser radiation as well as Rayleigh scatter. Analyses were performed with a varying laser power of ~1 to 15 mW depending on the analysed mineral phase and the slit aperture set to 20 μm in a high confocality setting. A 100× objective and a 2400 L/mm grating were used for the analyses resulting in spatial and spectral resolution of ~1 μm and 1 cm^{-1}, respectively. Calibration of the spectrometer was based on the Si 520.5 ± 0.5 cm^{-1} peak. The spectra were recorded using the Wire 4.2 software in the aluminosilicate network domain (~100 to 1300 cm^{-1} Raman shifts), and the water domain (~3000 to 3800 cm^{-1}) was checked when needed. Acquisition times varied from 10 to 300 s depending on the laser power condition and the nature of the analysed mineral phase.

4 | PETROGRAPHY

Both eclogite samples display comparable petrography. A detailed description of the sample BR18 is presented in

15251314, 0, Downloaded from https://onlinelibrary.wiley.com/doi/10.1111/jmg.12733 by Cochrane France, Wiley Online Library on [03/06/2023]. See the Terms and Conditions (https://onlinelibrary.wiley.com/terms-and-conditions) on Wiley Online Library for rules of use; OA articles are governed by the applicable Creative Commons License

de Hoÿm de Marien et al. (2020). In summary, the textural relationships in both samples point to a peak mineral assemblage of garnet (g1), omphacite (cpx1), kyanite (ky), phengitic muscovite (mu), and accessory quartz (q), rutile (ru), sulphide, apatite, and zircon. Garnet 1 porphyroblasts are anhedral, up to 3 mm in diameter (Figure 3a). Numerous inclusions of epidote (ep1), amphibole (amp1), and rutile as well as scarcer inclusions of omphacite, kyanite, phengite, quartz, apatite, and zircon are present in garnet 1 (Figure 3b–d). Epidote (ep1) and amphibole (amp1) are common in garnet 1 core and mantle but lack in its rim. A thin (up to 250 μm thick) rim of garnet 2 (g2) overgrows garnet 1 and contains inclusions of amphibole (amp2; fig. 3 in de Hoÿm de Marien et al., 2020). Rare anhedral crystals of albite observed in the matrix are significantly

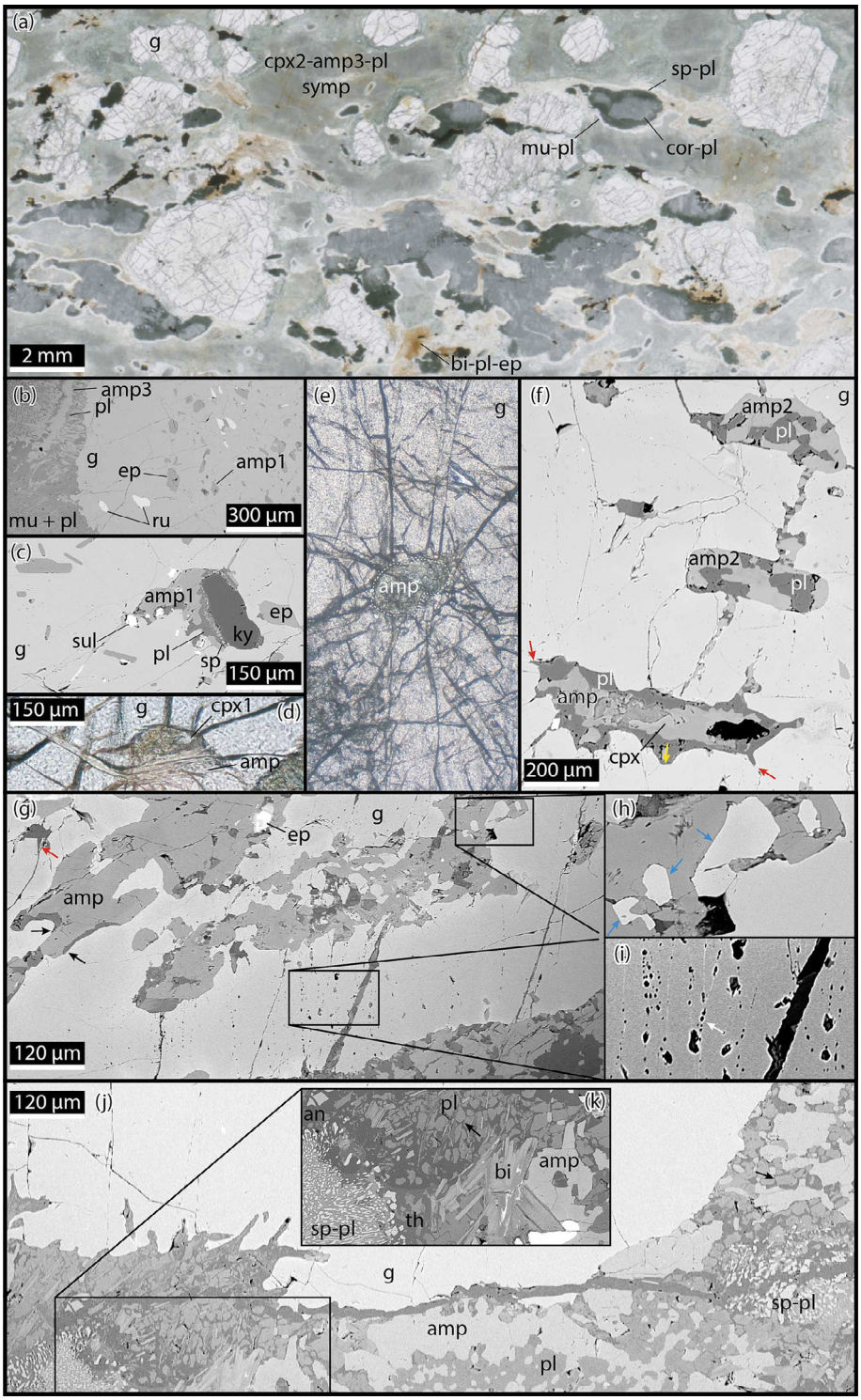

FIGURE 3 Photomicrographs and back-scattered electron images of the main textural features of the eclogites. (a) Photomicrograph of anhedral garnet crystals within a matrix of various symplectites after the eclogite facies minerals. Note that the shape of the corundum–spinel–plagioclase symplectites after kyanite shows a preferred orientation, but the crystals within the symplectites are undeformed. Garnet contains inclusions of (b) epidote, amphibole, and rutile; (c) kyanite; and (d) omphacite (cpx1). Garnet around the amphibole inclusions may be radially fractured (e). Amphibole inclusions are commonly associated with plagioclase (c, f, g). Note the presence of garnet crystals with straight grain boundaries with amphibole (blue arrows; h) and the alignment of small fluid inclusions, along sealed fractures in garnet (i). (j) Fracture filled by analcite (an) and thomsonite (th; centre) associated with biotite and rounded crystals of plagioclase close to spinel–plagioclase symplectite (left and right). At the vicinity of the fracture, garnet is dissolved and penetrated by channels also filled by analcite, thomsonite, and biotite. Note the interstitial character of analcite in (k). Red arrows indicate plagioclase offshoots within garnet, yellow arrow embayment in garnet, and black arrow plagioclase with low dihedral angle. [Colour figure can be viewed at wileyonlinelibrary.com]

15251314, 0, Downloaded from https://onlinelibrary.wiley.com/doi/10.1111/jmg.12733 by Cochrane France, Wiley Online Library on [03/06/2023]. See the Terms and Conditions (https://onlinelibrary.wiley.com/terms-and-conditions) on Wiley Online Library for rules of use; OA articles are governed by the applicable Creative Commons License

smaller (~100 μm) than garnet 1 but larger than the crystals in the matrix symplectites (~10 μm). They are inferred to be associated with garnet 2 because they are separated from the symplectites by a corona of diopside.

The matrix is mostly composed of various fine-grained symplectites (1 to 10 μm) that replace the peak metamorphic assemblage. Anhedral garnet are surrounded by a corona of amphibole (amp3) and plagioclase (pl). Matrix omphacite is replaced by fine-grained symplectites of diopside (cpx2), amphibole (amp3), plagioclase, and quartz. Kyanite is replaced by corundum–plagioclase and spinel–plagioclase symplectites, surrounded by an aureole of plagioclase locally containing small flakes of muscovite. Former phengitic muscovite is replaced by fine-grained aggregates involving biotite and low-Si muscovite. Rutile is surrounded by or juxtaposed to ilmenite, both being locally surrounded by a corona of titanite.

Many inclusions in garnet are large polymineralic inclusions with varied mineralogy but consistently containing plagioclase (Figure 3c,f,g). The shape of these inclusions is usually anhedral with locally complicated intergrowths between the host garnet and the inclusion (Figure 3g). Despite the overall anhedral shape of the inclusion, garnet locally forms isolated faceted crystals in contact with the inclusion (blue arrow in Figure 3h). At the contact with the polyinclusions, garnet has generally a modified composition (lower Mg and Ca and higher Fe and Mn; see X-Ray maps in Figure S1).

The individual crystals forming the inclusions are usually anhedral (Figure 3f). Their grain boundaries may be straight with the local presence of granoblastic texture (in Figure 3f—middle and top inclusions). In other cases, the grain boundaries are winding (Figure 3f—lower inclusion), and amphibole and clinopyroxene are rimmed by plagioclase at the contact with garnet. The garnet–plagioclase contact is curved. Plagioclase forms embayments and locally sharp offshoots along fractures within the host garnet (Figure 3f) as well as films with low dihedral angle terminations at the amphibole-garnet grain boundary (red arrows in Figures 3g and S2).

Garnet displays several sets of fractures. They are not systematically associated with inclusions, but garnet around the polyinclusions is always cracked. These fractures radiate around isolated inclusions (Figure 3e) or connect inclusion clusters (Figure 3f). The radial disposition of the fractures suggests a volume increase of the inclusions. Some fractures are filled with minerals similar to those of the neighbouring inclusion. Other fractures are healed with new garnet (white arrow in Figure 3g) and show fluid inclusion trails suggesting the presence of fluids possibly related to devolatilization.

Within the polyinclusions, the following mineral associations were observed: amphibole–plagioclase; amphibole–plagioclase–clinopyroxene; amphibole–plagioclase–corundum–spinel–K feldspar; amphibole–kyanite–plagioclase–spinel–sulphide; ilmenite–clinopyroxene–plagioclase–K feldspar–sulphide; K feldspar–plagioclase–orthopyroxene–titanite–calcite; and phengite–K feldspar.

Another set of fractures, cutting through both the garnet and the symplectitic matrix and filled by analcite, is locally observed (Figure 3j). Pools filled with analcite, thomsonite (a zeolite group mineral), subordinate plagioclase, and biotite developed along the fractures. Plagioclase is rounded, and biotite forms partially chloritized flakes. The pools are observed in the vicinity of the sp–cor–pl symplectites after kyanite where the Ca-rich plagioclase of the symplectites is embayed by analcite and thomsonite (Figure 3k). When the fractures occur next to garnet, the latter is penetrated by offshoots also filled by analcite, thomsonite, biotite, and plagioclase (Figure 3j).

5 | GEOCHEMISTRY

The samples have a basaltic composition (SiO_2 = 46.9–46.4%) with high Al_2O_3 (19.9–17.7%) and CaO (10.8–10.2%) contents. Both samples show enrichment in the most incompatible elements marked by a positive $(Nb/Yb)_N$ ratio (4–6; Figure 4a). However, BR19 is strongly depleted in Th and light rare-earth elements (LREE) with respect to BR18. This difference approaches an order of magnitude, resulting in an apparent Nb anomaly that is either slightly negative in BR18 or positive in BR19 (Figure 4a). This could suggest contrasting petrogenesis of the two samples, which is surprising given the identical sampling locality, comparable mineralogy, and major-element geochemistry. Alternatively, however, it could also point to the modification of one sample with respect to the other. Indeed, whereas Th and LREE are mostly immobile with respect to fluid alteration, they are mobile in melts (Klimm et al., 2008; Luginbühl, 2015), which could suggest that BR19 was depleted in melt with respect to BR18. This is consistent with the inferred presence of melt in the samples, the *P*–*T* evolution, as well as the typical igneous textures of some metamorphic zircons (see below).

The differences between the two samples may be further illustrated with chondrite-normalized REE patterns (Figure 4b). BR18 shows an overall higher REE concentration (ΣREE—BR18: 56.61 ppm; BR19: 18.54 ppm) and a negative slope of the chondrite-normalized pattern stronger than BR19. The difference between the two samples is best shown when BR19 is normalized with respect to BR18 (Figure 4c). According to the resulting pattern,

15251314, 0, Downloaded from https://onlinelibrary.wiley.com/doi/10.1111/jmg.12733 by Cochrane France, Wiley Online Library on [03/06/2023]. See the Terms and Conditions (https://onlinelibrary.wiley.com/terms-and-conditions) on Wiley Online Library for rules of use; OA articles are governed by the applicable Creative Commons License

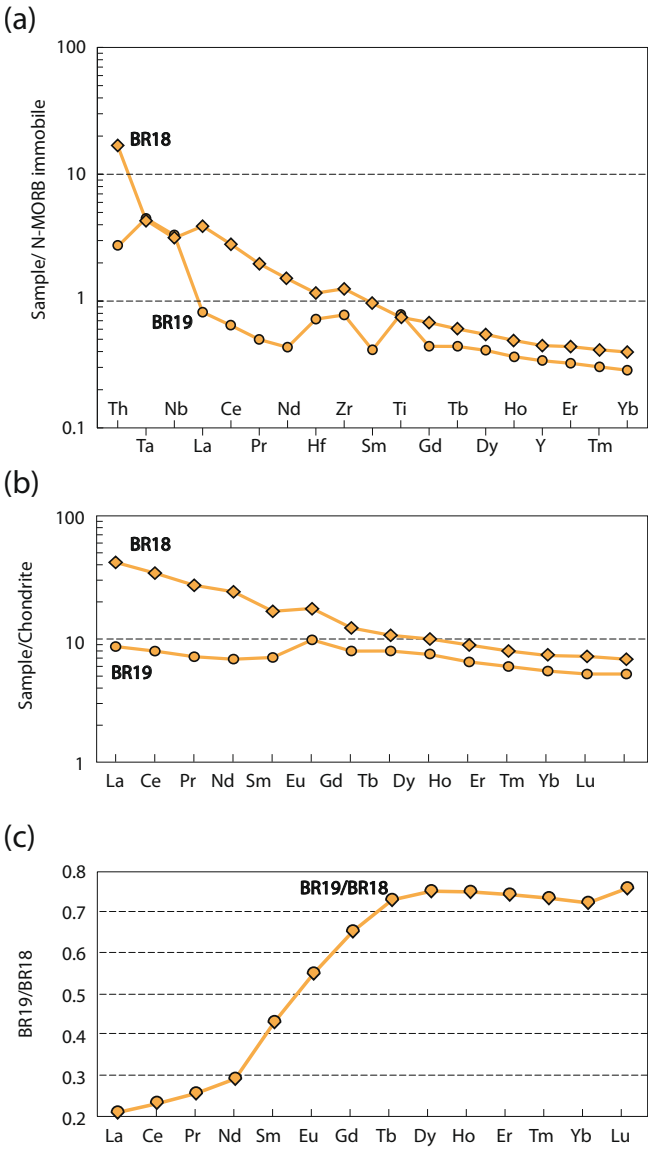

FIGURE 4 Geochemical plots. (a) Immobile-element N-MORB-normalized spidergram. (b) Chondrite-normalized rare-earth elements pattern. Note the depleted pattern of BR19 relative to BR18. (c) Sample/sample-normalized rare earth element pattern. This pattern is very similar to eclogite residue after partial melting documented by Wang et al. (2014). The plots were generated with GCDKit (Janoušek et al., 2006). Normalizing chondritic and N-MORB values after Sun and McDonough (1989). [Colour figure can be viewed at wileyonlinelibrary.com]

BR19 displays significantly lower LREE from La to Nd, and the magnitude of the difference rapidly decreases between Nd and Tb and is minimum in heavy rare-earth elements (HREE) between Tb and Lu. This pattern compares perfectly with that presented by Wang et al. (2014, their fig. 7d) for a restite after eclogite facies melting, suggesting again that partial melting in the eclogite facies and subsequent melt loss could account for the chemical composition of BR19.

6 | GEOCHRONOLOGY

Zircon, apatite, and rutile were selected for geochronology because they are characterized by significantly different closure temperatures and may consequently provide geochronological constraints on distinct thermal events or parts of the *P–T* history. In this study, the rather straightforward results obtained on apatite and rutile are used to interpret the more complex results obtained on zircon and are consequently presented first. For comparison, zircon and apatite from the felsic sillimanite-bearing diatexite, which encloses the eclogite lenses, were also analysed, and the results are presented in Supporting Information S1 (section "Geochronology of the embedding migmatite" including Figures S5–S8).

6.1 | Apatite

Apatite is common in the matrix of both samples and can be occasionally found as inclusions either in garnet (Figure 5a) or zircon. In the matrix, apatite occurs as millimetre-sized aggregates of subhedral crystals 200–500 μm long (Figure 5b). These aggregates are elongated and parallel with the fabric marked by former kyanite crystals. Under transmitted light, separated crystals are limpid and locally contain tiny inclusions. Under CL, apatite crystals are homogeneous at the scale of a single grain, but the colour of the whole population is variable (Figure 5c), reflecting variation in trace element contents.

Seventy-two analyses were performed on 33 crystals hand-picked from BR18 and 40 analyses on 21 crystals hand-picked from BR19. Apatite in BR18 has a variable U content (0.1–84 ppm; av = 20 ppm; Supporting Information S3, sheet #10), higher than BR19 (0.1–4 ppm; av = 1.37 ppm; Supporting Information S3, sheet #11).

Apatite separates analysed from the two eclogites yield homogeneous results. In a Tera–Wasserburg diagram, the data plot in a discordant position indicative of a significant proportion of common Pb (Figure 6a,b), higher in BR19 than in BR18. Characterization of the whole population together with repeated measurement of the grains with higher U contents in BR18 allows to define a discordia yielding a lower intercept date of 353 ± 1.5 Ma (MSWD = 1.4, n = 72) with a $^{207}Pb/^{206}Pb$ initial value of 0.857 ± 0.002 (Figure 6a). The spots in apatite grains from the sample BR19 define a less precise lower intercept date of 355 ± 12.5 Ma (MSWD = 1.2, n = 40) with a $^{207}Pb/^{206}Pb$ initial value of 0.856 ± 0.003 (Figure 6b). Both $^{207}Pb/^{206}Pb$ initial values are in a good agreement with the $^{207}Pb/^{206}Pb$ value of 0.859 calculated following the Pb evolution model of Stacey and Kramers (1975) for an age of 355 Ma. These dates are comparable

15251314, 0, Downloaded from https://onlinelibrary.wiley.com/doi/10.1111/jmg.12733 by Cochrane France, Wiley Online Library on [03/06/2023]. See the Terms and Conditions (https://onlinelibrary.wiley.com/terms-and-conditions) on Wiley Online Library for rules of use; OA articles are governed by the applicable Creative Commons License

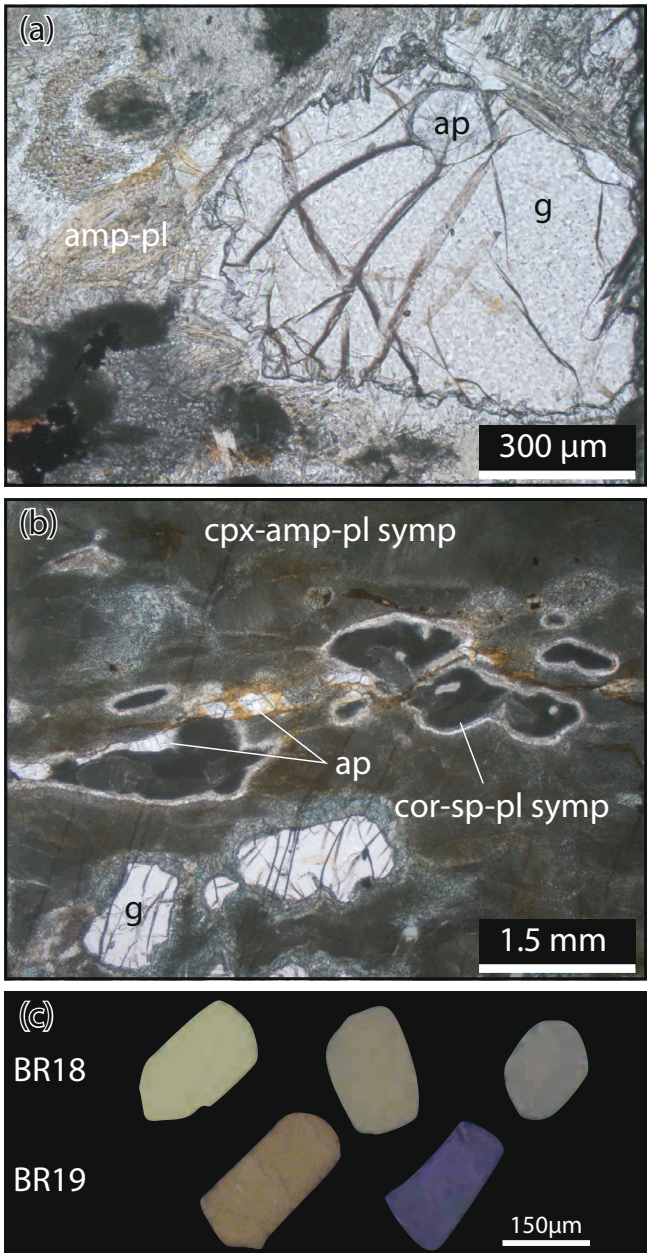

FIGURE 5 Photomicrographs (PPL) of an apatite inclusion in garnet (sample BR18) (a) and an apatite cluster-oriented parallel with former kyanite crystals (sample BR18) (b).
(c) Cathodoluminescence images of separated apatite crystals.
[Colour figure can be viewed at wileyonlinelibrary.com]

within error with the lower intercept date of 346 ± 5 Ma (MSWD = 0.86, $n = 24$) with a $^{207}Pb/^{206}Pb$ initial value of 0.826 ± 0.017 obtained on apatite from the surrounding migmatites (Figure S8).

6.2 | Rutile

Rutile is common both in the matrix and as inclusions in garnet (Figure 7a–d). The crystals are anhedral with size

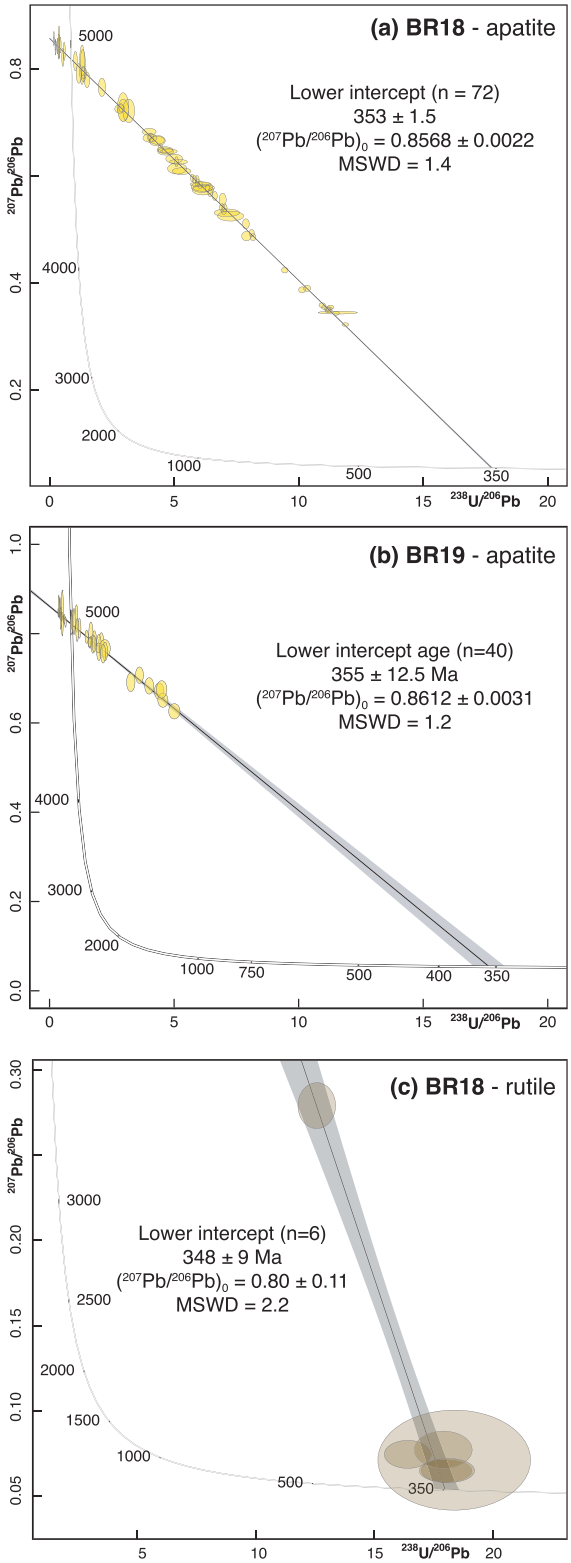

FIGURE 6 Tera–Wasserburg plots of U–Pb data from apatite from samples BR18 (a) and BR19 (b) and rutile from BR18 (c).
[Colour figure can be viewed at wileyonlinelibrary.com]

ranging from 50 to 250 µm. Forty-two in-situ analyses were performed on 18 grains directly in-context in thin section. U and Pb contents are low (U = 0.03–34.3 ppm,

15251314, 0, Downloaded from https://onlinelibrary.wiley.com/doi/10.1111/jmg.12733 by Cochrane France, Wiley Online Library on [03/06/2023]. See the Terms and Conditions (https://onlinelibrary.wiley.com/terms-and-conditions) on Wiley Online Library for rules of use; OA articles are governed by the applicable Creative Commons License

av = 2.0; Pb = 0.01–3.3 ppm; av = 0.2) whatever their textural positions. Zirconium contents vary from 137 to 362 ppm with an average of 250 ppm.

Rutile was analysed only in BR18. Forty-two analyses were performed directly in-context in thin section on 17 different rutile crystals with distinct textural positions. Because of low U and Pb contents in most grains, only six analyses from four different rutile grains found in the matrix could be used for geochronological purpose. Plotted in a Tera–Wasserburg diagram, the data are discordant indicating the presence of various amounts of common Pb (Figure 6c). A lower intercept date of

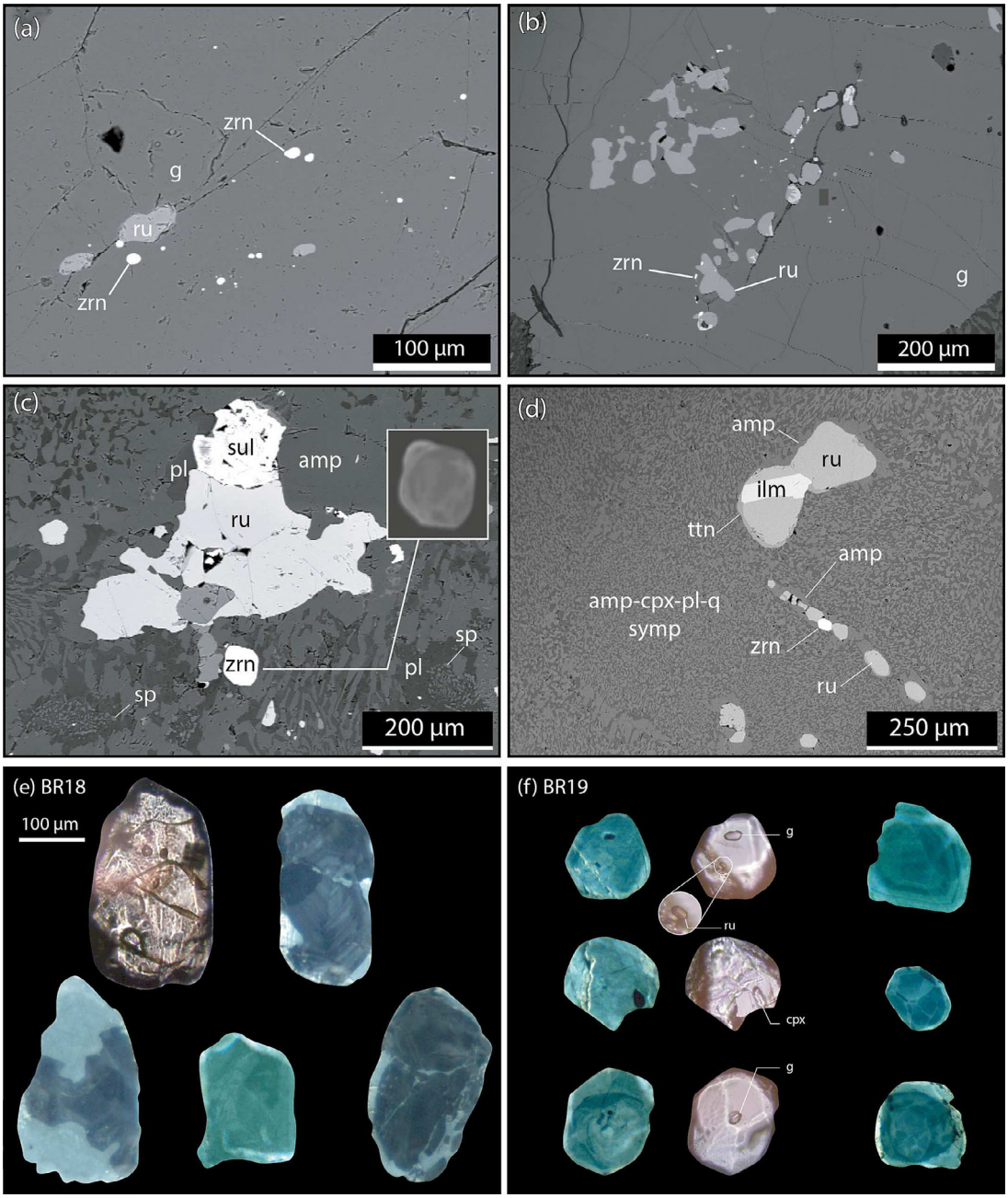

FIGURE 7 Zircon internal textures and textural relations. (a, b) Back-scattered electron images of zircon included in garnet. Note the spaced coronitic textures of zircon around rutile in (b). (c, d) Back-scattered electron images of zircon associated with rutile in the matrix. Inset in (c) is a cathodoluminescence (CL) image of the zircon. Compare (a) and (b) and (c) and (d) and note that numerous tiny zircons are included in garnet but single and larger zircons are observed in the matrix. (e, f) CL images and photomicrographs of selected zircons. (e) Note that the CL-bright zircon forms rims and embayments or seals fractures in the CL-dark zircon domains. CL-bright crystals are present in both samples. (f) Note the coexistence of patchy or flow textures, sector, and oscillatory growth zoning in the CL-bright zircons. Microinclusions were determined by Raman spectroscopy. [Colour figure can be viewed at wileyonlinelibrary.com]

15251314, 0, Downloaded from https://onlinelibrary.wiley.com/doi/10.1111/jmg.12733 by Cochrane France, Wiley Online Library on [03/06/2023]. See the Terms and Conditions (https://onlinelibrary.wiley.com/terms-and-conditions) on Wiley Online Library for rules of use; OA articles are governed by the applicable Creative Commons License

348 ± 9 Ma can be calculated (MSWD = 2.2, $n = 6$) yielding an initial $^{207}Pb/^{206}Pb$ ratio of 0.80 ± 0.11, compatible with the $^{207}Pb/^{206}Pb$ value of 0.859 calculated following the Pb evolution model of Stacey and Kramers (1975) for an age of 350 Ma.

6.3 | Zircon

Textural relationships between zircon and other minerals were investigated optically directly in thin section and through successful identification of 23 microinclusions out of over ~100 analyses carried out by Raman spectroscopy on ~250 zircon crystals separated and mounted in epoxy. Internal textures were investigated by CL imaging. Each zircon internal domain was analysed for trace elements and U–Pb isotopes. Potential control of zircon position (e.g., in garnet or in the matrix) on U–Pb results was also checked by performing analyses directly in-context in thin section.

A first population of zircon crystals is characterized by CL-dark cores that show in general patchy zoning but may be unzoned or display oscillatory growth zoning. These cores are surrounded by CL-bright rims; the interface between the dark cores and the bright rims is irregular, commonly convex towards the cores and cutting across the oscillatory zoning when present. CL-bright zones also form along cracks and around inclusions within the CL-dark zones. The zircon crystals are in general yellowish, cracked, and inclusion-rich and display stocky rounded habitus (Figure 7e), although translucent elongated crystals have also been observed. They represent ~75% of the zircon population in BR18, but only ~10–15% in BR19.

Zircon crystals from the second population are in the vast majority rounded, colourless, and translucent and contain few minute (up to 50 μm) faceted inclusions (Figure 7f). Compared with the zircons from the first population, they are less fractured but may contain few discrete and thin fractures. Trails of minute (~1 μm) inclusions can be observed in the extension of the fractures suggesting that the zircon crystals may have partially healed after fracturing (Figure 8). However, the fractures are not distinguishable under CL, possibly because the contrast is not strong enough. Under CL, these zircon grains are bright, comparable with the rims of the crystals of the first population (Figure 7e,f). They display various internal textures that encompass flow textures, patchy, oscillatory, or sector zoning (Figure 7f). Zircon crystals with flow textures are common and in general contain inclusions, whereas those with oscillatory or sector zoning are rarer and generally inclusion-free. In thin section, CL-bright zircon is commonly associated

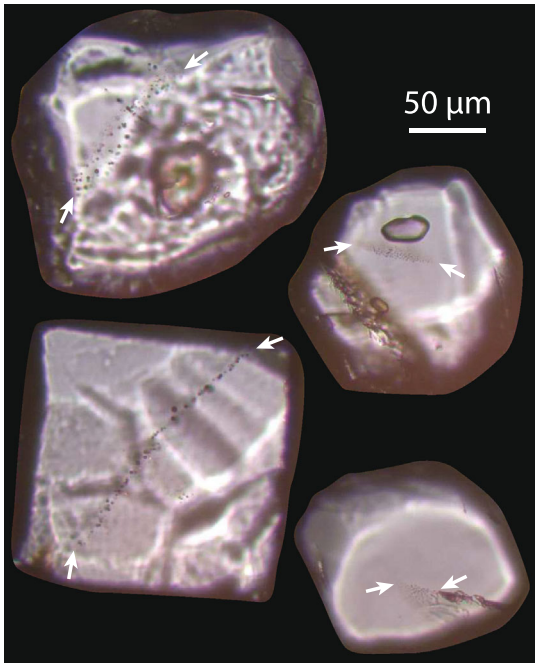

FIGURE 8 Photomicrograph (PPL) of planar inclusion trails in zircon. The white arrows mark the tip of the inclusion trails. [Colour figure can be viewed at wileyonlinelibrary.com]

with rutile, included in garnet, rutile, or in the cpx–amp–pl–q symplectites after omphacite. In garnet, zircon generally forms small clusters (Figure 7a) or trails of tiny and rounded crystals around inclusions of rutile (Figure 7b). By contrast, zircon associated with rutile in the matrix forms single larger crystals (Figure 7c,d). Raman spectroscopy investigation of inclusions in these CL-bright zircon crystals demonstrates mutual inclusion relationships with garnet ($n = 13$), rutile ($n = 5$), and clinopyroxene (possibly omphacite; $n = 2$) suggesting that these minerals crystallized contemporaneously. In addition, inclusions of apatite ($n = 1$), titanite corona around rutile in a cracked zircon ($n = 1$), hematite ($n = 1$), and a zigzag tubular-shaped feldspar ($n = 1$) were also determined.

The two zircon populations display contrasting trace-element characteristics well illustrated by chondrite-normalized (Boynton, 1984) trace-element patterns and in the Th/U versus Lu_N/Gd_N plot (Figure 9). The CL-dark sectors from BR18 display variable uranium content (114–556 ppm; av = 284 ppm), Th/U (0.44–2.16; av = 0.78), and REE contents (ΣREE = 251–1079 ppm). One spot displays similarities with the CL-bright zircons described below and is considered as an outlier. Chondrite-normalized REE patterns (Figure 9a) are characterized by negative Eu anomalies (Eu_N/Eu^* = 0.11–0.16; av = 0.26) and moderate HREE enrichment (Lu_N/Gd_N = 13–31; av = 21). Ti content is variable (2.5–15 ppm; av = 8 ppm).

15251314, 0, Downloaded from https://onlinelibrary.wiley.com/doi/10.1111/jmg.12733 by Cochrane France, Wiley Online Library on [03/06/2023]. See the Terms and Conditions (https://onlinelibrary.wiley.com/terms-and-conditions) on Wiley Online Library for rules of use; OA articles are governed by the applicable Creative Commons License

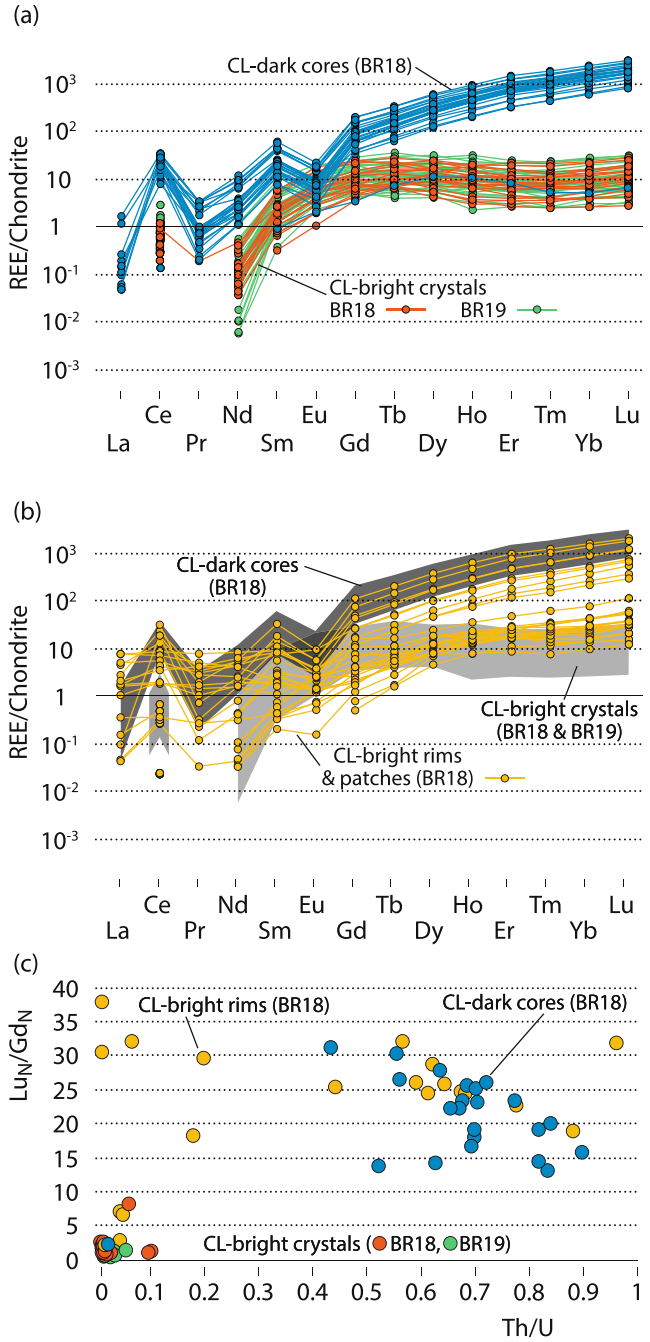

FIGURE 9 Trace-element characteristics of zircon. Chondrite-normalized trace-element patterns in the CL-dark cores and CL-bright crystals (a) and the CL-bright rims (b). (c) Lu_N/Gd_N versus Th/U plot of spots in BR18 showing two distinct end-members and scattering of spots in the CL-bright crystals. Same colours as (a) and (b). CL, cathodoluminescence; REE, rare earth element. [Colour figure can be viewed at wileyonlinelibrary.com]

CL-bright crystal domains display strikingly homogeneous chemical compositions in both samples. Compared with the CL-dark domains, they are characterized by lower U (BR18: 14–58 ppm, av = 28; BR19: 19–99 ppm, av = 47.5), Th/U ratios (BR18: 0.01–0.1, av = 0.03; BR19: 0.01–0.06, av = 0.02), and REE contents (BR18: 5.2–20.2 ppm, av = 11.3 ppm; BR19: 4.6–25.6 ppm, av = 11.3 ppm). Their chondrite-normalized REE patterns show average Eu anomalies close to unity (BR18: $Eu_N/Eu^* = 0.55–1.19$, av = 0.94; BR19: $Eu_N/Eu^* = 0.4–1.7$, av = 1.1) and flat HREE patterns (BR18: $Lu_N/Gd_N = 0.35–8$, av = 4; BR19: $Lu_N/Gd_N = 0.4–2.1$, av = 1.0). The Ti content is less variable than in the CL-dark sectors (BR18: Ti = 1.8–5.1 ppm, av = 3.2 ppm with one analysis at 20 ppm; BR19: Ti = 0.89–7.5 ppm, av = 3.73 ppm; with one analysis at 10 ppm).

The thin CL-bright rims or patches around or within the CL-dark domains display heterogeneous chemical characteristics intermediate between those resembling the CL-dark domains and the CL-bright crystals (Figure 9b) and may be considered in most cases as mixed analyses.

The isotopic results obtained using the small spot size (see Section 3) from each sample were plotted in two Tera–Wasserburg diagrams (Figures 10a,b) except for spots with high analytical errors. Data obtained in BR18 are dispersed but form two main clusters of concordant to slightly discordant analyses c. 500 and c. 350 Ma. Data from the CL-dark domains are shown in deep blue and compose the c. 500 Ma cluster, although a few spots plot in younger positions, down to c. 400 Ma. An apparent age of 490 ± 3 Ma ($MSWD_{C+E} = 1.6$; $n = 19$; Figure 11) can be calculated using the data from the main cluster. In BR19, the only spot obtained in a CL-dark zircon domain yields a younger apparent age of 420 Ma suggesting mixing with an underlying CL-bright domain. Data obtained in the CL-bright zircons from both samples (red and orange ellipses in Figure 10a,b) cluster at c. 350 Ma close to the apparent age obtained on apatite (see above). Results for the spots from the CL-bright rims analysed in BR18 are shown in light blue (Figure 10a). They plot in a concordant to very discordant position and strongly scatter, mostly between the two main clusters, but they may also plot in older positions.

CL-bright zircon crystals commonly yield apparent ages (350–320 Ma) equivalent to or even younger than apatite (c. 355–350 Ma), which is commonly not expected (see discussion below). Despite the important cluster c. 350 Ma (Figure 10b), zircon data scatter between c. 380 and 320 Ma suggesting a more complex distribution of the age data that could be disclosed through greater precision on individual spots. Consequently, both the CL-bright crystals from sample BR18 already characterized for trace elements, and the zircon grains in thin sections were (re)analysed using a larger beam size in order to ensure the ablation of a larger volume of material (almost four times). The resulting data are equivalent (Figure 10c) to the ones obtained with small spot size but

15251314, 0, Downloaded from https://onlinelibrary.wiley.com/doi/10.1111/jmg.12733 by Cochrane France, Wiley Online Library on [03/06/2023]. See the Terms and Conditions (https://onlinelibrary.wiley.com/terms-and-conditions) on Wiley Online Library for rules of use; OA articles are governed by the applicable Creative Commons License

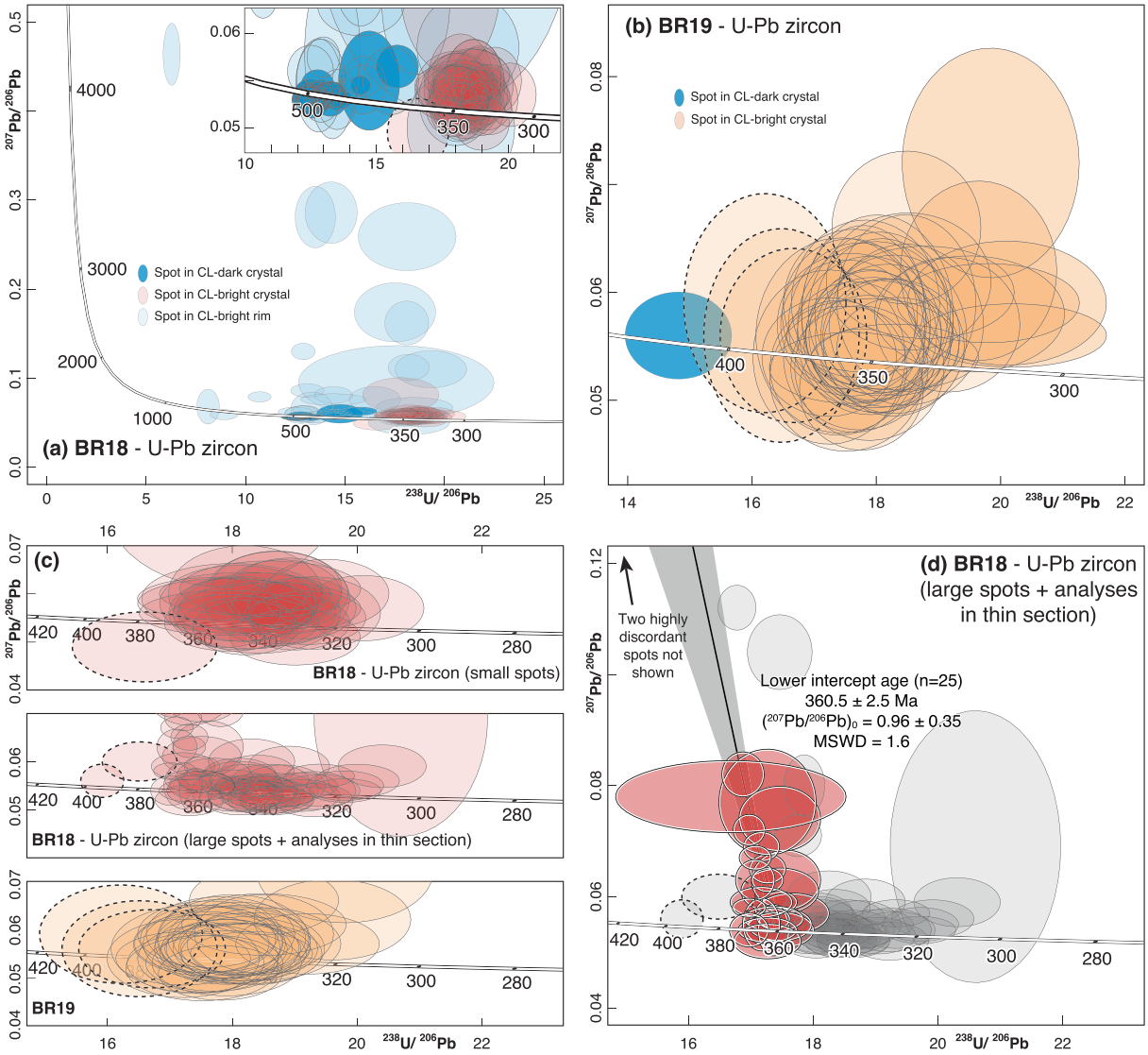

FIGURE 10 Tera–Wasserburg plots of zircon U–Pb data. (a) All zircon data from BR18 and zoom on the two main cluster. (b) All zircon data from BR19. (c) Comparison between the data obtained in BR18 with small spots (top plot), large spots and analyses in thin section (middle plot), and in BR19 (bottom plot). (d) Zircon data obtained using large spot size and directly in thin section. The ellipses coloured in red are used to calculate the lower intercept age. Note also the important spread along the concordia (grey ellipse with thin contour), the scarce apparently older spots (grey ellipses with dashed contour), and that two highly discordant spots (that are not used in the calculation of the discordia) are not shown. CL, cathodoluminescence. [Colour figure can be viewed at wileyonlinelibrary.com]

display a better individual analytic precision. Data obtained directly in thin section do not reveal any clear textural control and are shown in the same figure. Figure 10d shows that the main cluster of concordant to slightly discordant spots plots again between c. 350 and 320 Ma. A secondary population of concordant and discordant spots (red coloured ellipses) plots along a discordia yielding a lower intercept date of 360.5 ± 2.5 Ma (MSWD = 1.6; $n = 25$) and pointing to an initial Pb isotopic composition of 0.96 ± 0.35. Despite the large error, this initial Pb isotopic composition is broadly consistent with the $^{207}Pb/^{206}Pb$ value of 0.8597 calculated following the terrestrial Pb evolution model of Stacey and Kramers (1975) for an age of 360 Ma. Apart from two older spots c. 390–380 Ma (dashed-rim ellipses), the rest of the data plots in a younger position (down to c. 310 Ma).

A weighted mean $^{206}Pb/^{238}U$ apparent age of 360.5 ± 1.5 Ma (MSWD = 1.1; $n = 16$; Figure 11) can be calculated using only the concordant analyses (concordance >90%) out of the data aligned along the discordia. Most of the other data spread along the concordia curve from c. 350 to c. 310 Ma, and three older spots yield an apparent weighted mean age of 370 ± 3.5 Ma (MSWD = 1.0). The data set obtained in

15251314, 0, Downloaded from https://onlinelibrary.wiley.com/doi/10.1111/jmg.12733 by Cochrane France, Wiley Online Library on [03/06/2023]. See the Terms and Conditions (https://onlinelibrary.wiley.com/terms-and-conditions) on Wiley Online Library for rules of use; OA articles are governed by the applicable Creative Commons License

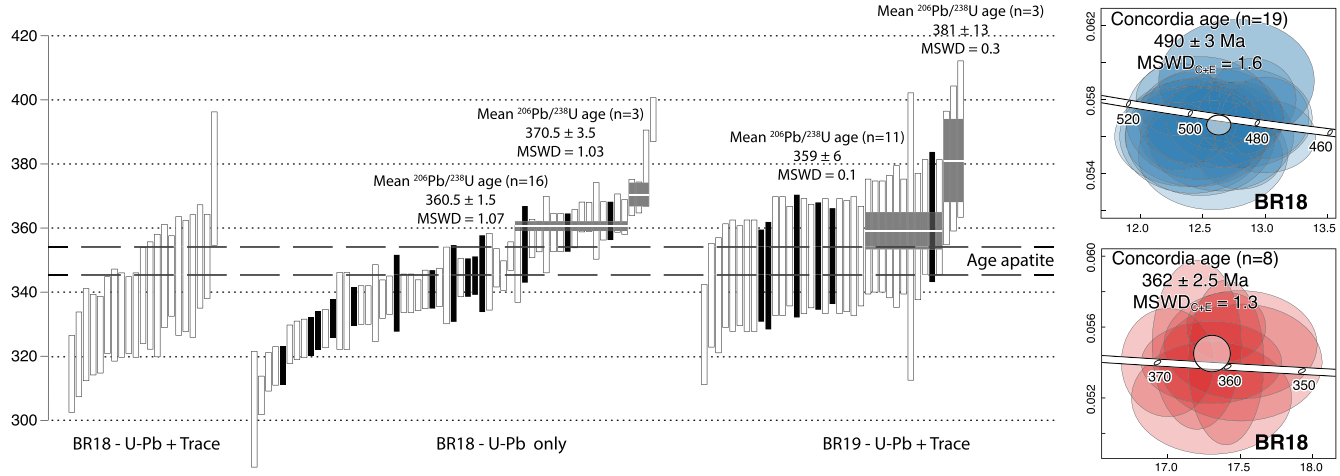

FIGURE 11 Weighted mean average and concordia age plots of the U–Pb data in zircon. The long-dashed lines on the weighted mean average plot correspond to the interval of the discordia ages obtained from apatite. Analyses in zircons with flow textures are shown as white bars and those with oscillatory and sector zoning as black bars. The concordia ages have been calculated using the data obtained in the cathodoluminescence-dark zircon cores (blue ellipses) and the cathodoluminescence-bright crystals (red ellipses). $MSWD_{C+E}$ for concordance + equivalence. [Colour figure can be viewed at wileyonlinelibrary.com]

the other sample (BR19) displays an overlap between individual analyses due to the small size of the analytical spots and does not bring a clear geochronological information. However, apparent ages comparable with the results of BR18 can be calculated. The three oldest spots yield an apparent age of c. 381 Ma. Within the main population, the oldest spots allow the calculation of an apparent age of c. 360 Ma (Figure 11).

7 | THERMOMETRY

The coeval crystallization of zircon, rutile, and quartz, inferred above and supported by the mutual inclusion relations, and the inclusion of all three minerals in garnet, is suitable for the application of the Zr-in-rutile and Ti-in-zircon geothermometry. The pressure-dependent calibrations of Hofmann et al. (2014) and Tomkins et al. (2007) were applied to the CL-bright zircon domains and rutile, respectively.

Ti-in-zircon and Zr-in-rutile data were checked for systematic trends with respect to the position of the spot in a single crystal and for textural control in thin section, but no correlation could be observed. The thermometry results were plotted against P and T using the minimum and maximum values of Ti in zircon and Zr in rutile (Figure 12). Ti in zircon from BR19 yields temperatures between 600°C and 850°C (at $P > 19$ kbar), a wide interval that encompasses the whole temperature range modelled for the eclogite and granulite facies metamorphism (de Hoÿm de Marien et al., 2020). The results obtained on zircon from BR18 indicate a narrower range of temperatures ($T = 770$–

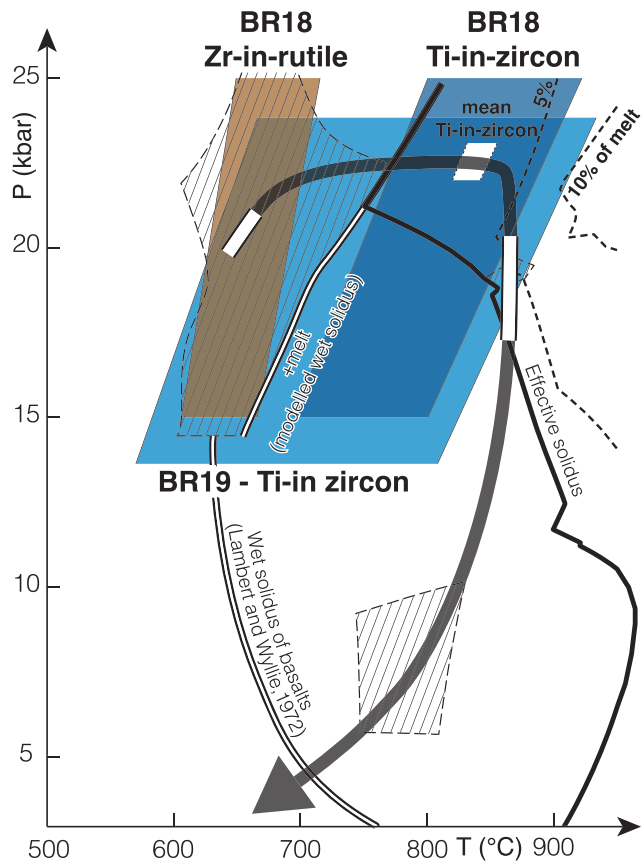

FIGURE 12 Ti-in-zircon and Zr-in-rutile thermometry results. The P–T path is drawn after pseudosection modelling in de Hoÿm de Marien et al. (2020). The hatched areas correspond to the stability fields of the critical mineral assemblages. White portions on the P–T path indicate recognized periods of zircon growth. [Colour figure can be viewed at wileyonlinelibrary.com]

15251314, 0, Downloaded from https://onlinelibrary.wiley.com/doi/10.1111/jmg.12733 by Cochrane France, Wiley Online Library on [03/06/2023]. See the Terms and Conditions (https://onlinelibrary.wiley.com/terms-and-conditions) on Wiley Online Library for rules of use; OA articles are governed by the applicable Creative Commons License

860°C at $P = 20$–22.5 kbar, inferred from the phase-diagram modelling) above the modelled solidus of the sample. Application of the thermometer using the averaged Ti-in-zircon content results in temperatures of 833 ± 15°C and 845 ± 10°C for BR18 and BR19, respectively. Minimum and maximum Ti-in-rutile thermometry results intersect with the *P*–*T* path between ~620°C and ~700°C ($P > 19$ kbar) corresponding to the conditions of crystallization of the garnet cores (de Hoÿm de Marien et al., 2020).

8 | INTERPRETATION OF THE POLYMINERALIC INCLUSIONS

The studied eclogites have been inferred to have undergone partial melting during the peak temperature part of their evolution (de Hoÿm de Marien et al., 2020; Figure 12). Additional arguments are presented here, because the presence of melt is important for the interpretation of the geochronological and geochemical data, as zircon or apatite might have interacted with or crystallized directly from the melt (e.g., Harley et al., 2007; Yakymchuk et al., 2019) and the geochemical signature of the samples may have been modified by partial melting (e.g., Palin et al., 2016).

One of the interesting features of the studied eclogites is the presence of large polymineralic inclusions in garnet crystals. Such inclusions have been described from natural samples (e.g., Cao et al., 2020; Lang & Gilotti, 2007) and HT experiments (Perchuk et al., 2005, 2008) and were interpreted as the result of partial melting of primary monomineralic inclusions. In the present case, they may represent former inclusions of amphibole, entrapped during the prograde subsolidus growth of garnet. *P*–*T* pseudosection modelling of such amphibole melting (Figure S9) suggests the formation of peritectic garnet and clinopyroxene, in agreement with the observations, alongside with the recrystallization of amphibole. The presence of melt along grain boundaries is supported by the plagioclase films with low dihedral terminations (Figure 3g; black arrows), interpreted as melt pseudomorphs (e.g., Ferrero et al., 2012; Holness et al., 2011; Holness & Sawyer, 2008). The associated volume increase of the inclusions would account for the radial fractures in garnet.

9 | INTERPRETATION OF THE GEOCHRONOLOGICAL RESULTS

The textural relations described above suggest that all dated minerals, zircon, rutile, and apatite belong to the eclogite facies metamorphic stage. Whereas the geochronological record of zircon is relatively complex, it can be decrypted using the comparatively simple data from rutile and apatite.

Rutile and apatite from both samples yield a homogeneous, coherent apparent age of c. 350 Ma (350 ± 7.5, 353 ± 1.5, and 355 ± 12.5 Ma; Figure 6). The same date is also recorded by apatite from the surrounding felsic migmatite (346 ± 5 Ma; Figure S8). Although apatite belongs to the HP assemblage, it is reputed for a relatively low closure temperature for Pb diffusion (350–600°C; Chamberlain & Bowring, 2001; Cherniak et al., 1991; Cochrane et al., 2014; Harrison et al., 2002) and significant reactivity in the presence of fluids (e.g., Harlov, 2015). Because a significant part of the post-eclogite evolution occurred at high temperatures (750–850°C; Figure 12) and involved a fluid as indicated by the replacement of anhydrous omphacite and garnet by amphibole-bearing assemblages, the well-defined c. 350 Ma apparent ages of apatite are interpreted as the age of cooling.

Rutile also belongs to the HP assemblage in agreement with the results of thermodynamic modelling and Zr-in-rutile thermometry. However, the close apparent age and closure temperature of apatite and rutile (~600°C; Cherniak, 2000) suggest that the 350 ± 7.5 Ma apparent age obtained in rutile records the same cooling process (cf. Lotout et al., 2020).

Zircon, on the other hand, yields apparent ages both significantly older and younger than the rutile and apatite cooling age of c. 350 Ma (Figures 10 and 11). However, the closure temperature with respect to Pb diffusion in zircon (~900°C; e.g., Cherniak & Watson, 2001; Kramers et al., 2009; Lee et al., 1997) is higher than that of rutile and apatite and the maximum temperature reached by the rocks (~875°C, Figure 12). Consequently, the "young" apparent ages cannot be interpreted in terms of simple diffusive Pb loss.

The texturally oldest CL-dark zircon cores display internal textures including oscillatory growth zoning pointing to a magmatic origin (Corfu et al., 2003; Vavra, 1990) in agreement with the trace-element data showing Th/U > 0.1, negative Eu anomaly, and HREE-enriched REE patterns (e.g., Rubatto, 2002, 2017; Rubatto & Gebauer, 2000). The 490 ± 3 Ma concordia date obtained with these zircon crystals is accordingly interpreted as the crystallization age of the gabbroic protolith of the eclogite.

CL-bright zircon crystals consistently display low Th/U (<0.1), an absence of negative Eu anomaly, and a flat HREE pattern (Figure 9a) suggesting they are metamorphic and crystallized in the presence of garnet but absence of plagioclase (e.g., Rubatto, 2002, 2017), characteristics typical of the eclogite facies. They show two major groups of internal textures—flow textures versus

15251314, 0, Downloaded from https://onlinelibrary.wiley.com/doi/10.1111/jmg.12733 by Cochrane France, Wiley Online Library on [03/06/2023]. See the Terms and Conditions (https://onlinelibrary.wiley.com/terms-and-conditions) on Wiley Online Library for rules of use; OA articles are governed by the applicable Creative Commons License

oscillatory or sector zoning. Zircon crystals with flow textures commonly contain minute inclusions of rutile, garnet, and possibly omphacite, consistently with the trace-element data (Supporting Information S3; sheet #6). The inclusions are faceted and much smaller than the crystal size of the minerals of the eclogitic assemblage. This suggests that they were captured during an important nucleation stage likely related to the onset of the eclogite facies. This is consistent with Ti-in-zircon temperatures that span a large interval but may be as low as 630°C at 19 kbar. Furthermore, the crystallization of zircon along the prograde evolution is compatible with the observation of clusters or trails of zircon beads around rutile included in garnet, interpreted as a prograde product of destabilization of a magmatic ilmenite (cf. Beckman & Möller, 2018; Bingen et al., 2001). However, flow-textured zircons have been interpreted as modified primary zoning (Harley et al., 2007; Vavra et al., 1996). The large spread of apparent ages ranging from c. 380 to 310 Ma (with one older spot at c. 390 Ma) obtained from zircons with flow textures could be consequently interpreted in term of partial to total recrystallization of early eclogite facies crystals.

Zircon crystals with sector or oscillatory zoning are less common, mostly lack inclusions and show a slightly less important spread of apparent ages (c. 365–310 Ma, i.e., they do not yield the older ages recorded in the flow-textured crystals; Figure 11). This type of zoning is usually interpreted as pristine (Corfu et al., 2003; Harley et al., 2007; Rubatto, 2017; Vavra et al., 1996) igneous textures (Schaltegger et al., 1999; Vavra, 1990). It suggests that these grains crystallized from melt, which is compatible with the Ti-in-zircon thermometry results and the inferred *P–T* evolution of the studied samples in the presence of melt (Figure 12). As a general rule, in partially molten rocks, zircon grows during melt crystallization (e.g., Kelsey et al., 2008; Kohn et al., 2015). Along the *P–T* path of the eclogite (Figure 12), melt crystallizes during decompression at ~875°C and ~19 kbar, at the transition between the eclogite and the HP granulite facies, and it is inferred that the CL-bright oscillatory-zoned zircons crystallized at this stage. The oldest recorded apparent age (c. 360 Ma) could be associated with this crystallization event. However, many of these zircon domains yield apparent ages younger than the age of apatite (inferred to represent cooling below ~600°C) and must have undergone subsequent recrystallization.

Consequently, zircon ages older than apatite and rutile (i.e., older than 350 Ma) can be interpreted in terms of zircon crystallization along the prograde *P–T* path or at the eclogite facies peak, and further crystallization or recrystallization during the incipient decompression at high temperatures, in the presence of melt. The age of c. 360 Ma that can be calculated using different methods (cf. Figures 10 and 11) on both samples is the best estimate for the age of the eclogite facies *P–T* peak. On the other hand, apparent ages younger than c. 350 Ma must be attributed to the late cooling and associated retrogression of the eclogites. Because diffusion of radiogenic Pb is essentially impossible in zircon at these temperatures, the results are interpreted to reflect zircon recrystallization, which appears to preserve the REE signature while resetting the U–Pb system (cf. Hoskin & Black, 2000; Martin et al., 2008; Pitra et al., 2022; Schmädicke et al., 2018; Štípská et al., 2016). Zircon is known to readily recrystallize in the presence of hydrothermal fluids (e.g., Ayers et al., 2003; Geisler et al., 2007; Spandler et al., 2004), in particular if they have an alkaline character (e.g., Rubatto et al., 2008; Soman et al., 2010), from greenschist facies conditions (250–450°C; Chen & Zhou, 2017) up to the conditions of the granulite facies (750–1000°C; Taylor et al., 2014, and references therein). Such a process is consistent with the common presence of planar fluid-inclusion trails in zircon (Figure 8), which points to zircon fracturing and subsequent healing. The alkaline character of the fluids that interacted with the eclogite at low temperatures is supported by the occurrence of analcite and thompsonite in some of the fractures that cut through the rock. On the other hand, apatite is sensitive to alkaline fluids at high temperatures (700–900°C; Antignano & Manning, 2008), but the presence of Na in the fluid inhibits apatite recrystallization at low temperatures (Harlov, 2015; Harlov et al., 2002). The circulation of a relatively low-temperature sodic fluid during cooling then probably results in selective recrystallization of zircon, whereas apatite remained unaffected.

The apparent ages of these recrystallized zircon domains spread down to c. 310 Ma (Figures 10 and 11). Given the shape of the concordia curve in this time interval, a 360 Ma old zircon crystal affected by partial resetting at say 310 Ma would produce data that are concordant within error although the individual apparent ages are meaningless (Pitra et al., 2022). This could suggest that the youngest recorded date (c. 310 Ma) would reflect the maximum age of the fluid circulation. At the regional scale, these fluid circulations may be related to the widespread granitoid plutonism between c. 340 and c. 310 Ma (Laurent et al., 2017).

10 | GEOLOGICAL HISTORY OF THE LA BORIE ECLOGITE

The eclogites occur closely associated with biotite–sillimanite metatexites, felsic diatexites, and migmatitic felsic orthogneisses suggesting emplacement of the

15251314, 0, Downloaded from https://onlinelibrary.wiley.com/doi/10.1111/jmg.12733 by Cochrane France, Wiley Online Library on [03/06/2023]. See the Terms and Conditions (https://onlinelibrary.wiley.com/terms-and-conditions) on Wiley Online Library for rules of use; OA articles are governed by the applicable Creative Commons License

protolith in a continental setting rather than a mature oceanic domain. U–Pb dating of the magmatic core of zircons indicates that the protolith was emplaced during the late Cambrian (490 ± 3 Ma). This event can be related to the thinning and fragmentation, accompanied by widespread bimodal magmatism, that affected the northern margin of Gondwana during the Cambrian and Ordovician (e.g., Ballèvre et al., 2012; Chelle-Michou et al., 2017; Košler et al., 2004; Linnemann et al., 2008; Lotout et al., 2017; Paquette et al., 2017; Sánchez-García et al., 2003).

After the protolith emplacement, the samples lack chronological or petrological record until the onset of the high-pressure metamorphism. The earliest metamorphic record is found as garnet cores that crystallized ~650°C, 20 kbar (Figure 12; de Hoÿm de Marien et al., 2020). The breakdown of magmatic ilmenite to rutile occurred around the same time as indicated by the results of Zr-in-rutile thermometry (~620–700°C) and was accompanied by the formation of first metamorphic zircon (Figure 7a,b). This possibly corresponds to the oldest ages recorded in the metamorphic zircon (c. 380–370 Ma). Metamorphic zircons subsequently recrystallized during the prograde metamorphism documented otherwise by the growth and chemical zoning of garnet porphyroblasts. Garnet zoning suggests an initial pressure and temperature increase to 700°C, 22–23 kbar prior to a roughly isobaric temperature increase likely up to 875°C, associated with partial melting (de Hoÿm de Marien et al., 2020). At this moment, amphibole inclusions in garnet partially melted resulting in the formation of polyinclusions with features such as plagioclase pseudomorphs after melt films along grain boundaries. The high temperature recorded by the Ti-in-zircon thermometry (up to ~875°C) points to a major recrystallization of the pre-existing zircons during this stage, close to the peak *P–T* conditions. This recrystallization event was accompanied or closely followed by progressive crystallization of the melt and the concomitant formation of new zircon with igneous textures at c. 360 Ma. Overgrowth of new garnet around the eclogitic garnet is associated with incipient crystallization of plagioclase in the matrix and records decompression in the HP granulite facies. Further decompression is marked by the pervasive replacement of matrix omphacite by HT amphibole–plagioclase symplectites ~750–850°C and less than 9 kbar. During subsequent cooling, the U–Pb system of apatite and rutile closed c. 350 Ma. Later lower-temperature fluid infiltration promoted a major recrystallization of the zircon crystals at c. 310 Ma or younger. Hence, important decompression and subsequent cooling were achieved c. 10 Ma after the peak *P–T* conditions.

11 | TECTONIC IMPLICATIONS

The results obtained in the studied eclogites document the emplacement of the protoliths during a late Cambrian (c. 490 Ma) rifting of a continental margin, subsequently subducted in the late Devonian (c. 370–360 Ma), partly exhumed during the early Carboniferous (c. 350 Ma) and finally affected by late hydrothermal alteration (possibly at c. 310 Ma or later). Our results do not reproduce the Silurian age for the eclogite facies metamorphism, and this age must consequently be abandoned in the tectonic reconstructions as already proposed by other authors (Benmammar et al., 2020; Lotout et al., 2018, 2020; Paquette et al., 2017).

The Devonian age obtained from the studied eclogite is equivalent to the age obtained in other eclogites associated with migmatites in southern parts of the FMC (Lotout et al., 2020; Pitra et al., 2022). Overall, the results show that the Variscan subduction in the Massif Central was much shorter than previously thought (max. 20 Ma instead of ~70 Ma) and do not support any significant north–south diachrony of the HP metamorphism (cf. Figure 1b).

11.1 | Implications for the tectonic evolution of the FMC

Our data show that the age of the eclogite-facies metamorphism in the UGU (c. 360 Ma) is equivalent to the age of the suprasubduction calc-alkaline magmatism in the Morvan and Brévenne areas pointing to a possible genetic relationship (Figure S10). This suggests that the basement of the Morvan and Brévenne areas represents a part of the Devonian upper plate rather than a piece of the UGU (lower plate). It can be proposed that the thinning of the arc domain in the Brévenne area and the associated magmatism have been produced by the retreat of a subducting slab at c. 360 Ma. This was contemporaneous with the incipient decompression following melting at the eclogite facies peak. Partial melting of the subducted rocks could have triggered their detachment from the subducting slab (Labrousse et al., 2011; Závada et al., 2018) and account for the onset of the exhumation of the eclogites that reached crustal conditions shortly after (c. 350 Ma).

As mentioned above, the magmatic rocks of the Morvan and Brévenne areas display a regional lithological zoning from andesite in the north (Morvan) to the bimodal spillite–keratophyre association in the south (Brévenne). This lithological zoning is associated with southward decreasing enrichment in incompatible elements of these magmatic rocks, suggesting their emplacement during a southward subduction (Pin et al., 1982; Pin & Paquette, 2002; Figure 13). The Morvan would

15251314, 0, Downloaded from https://onlinelibrary.wiley.com/doi/10.1111/jmg.12733 by Cochrane France, Wiley Online Library on [03/06/2023]. See the Terms and Conditions (https://onlinelibrary.wiley.com/terms-and-conditions) on Wiley Online Library for rules of use; OA articles are governed by the applicable Creative Commons License

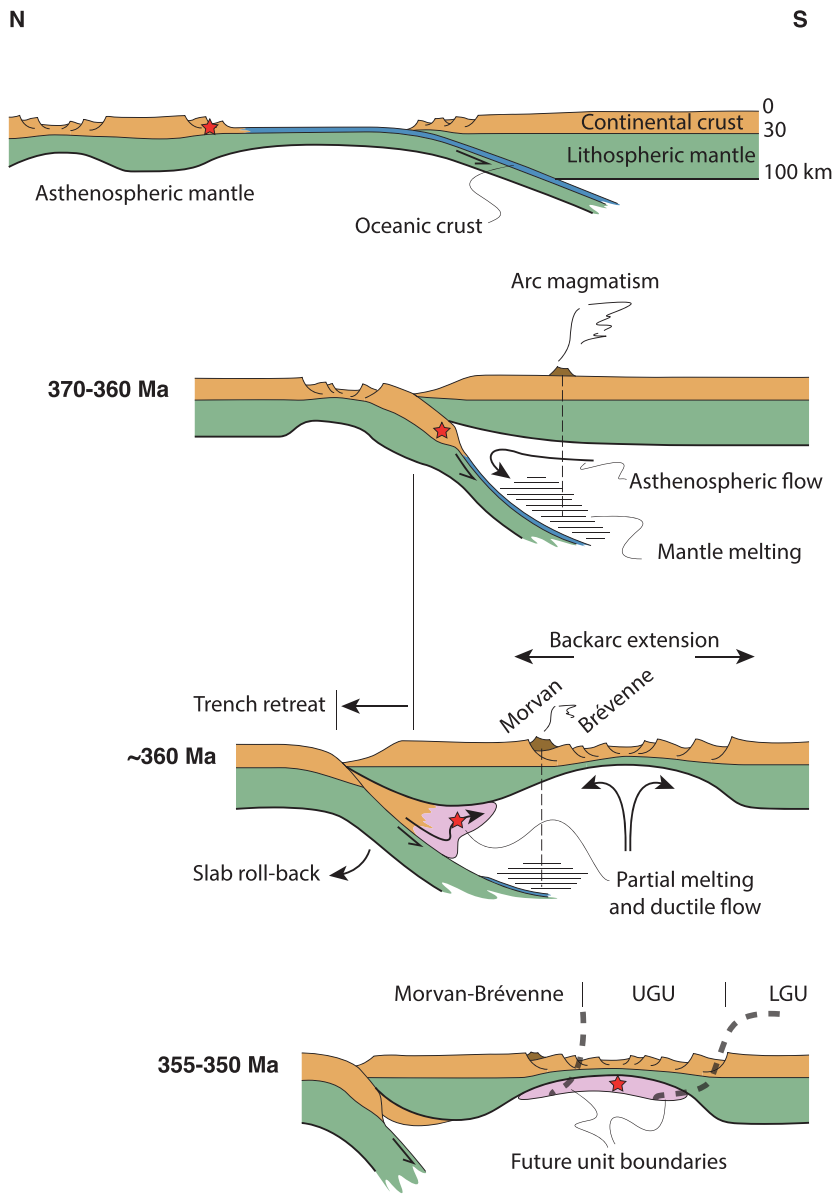

FIGURE 13 Sketch of the Devonian to early Carboniferous evolution of the French Massif Central. The red star represents the studied eclogite. Following subduction (>370 Ma) and the arrival of buoyant continental crust in the subduction zone, the slab steepens providing space for asthenospheric flow (~370) resulting in heating of the subducted crust up to partial melting and incipient upward detachment from the subducting slab (360 Ma). Note the contemporaneous development of the arc magmatism (Morvan). Detachment of the buoyant crust from the subducting lithosphere results in shallowing the dip of the slab by moving the trench towards the subducting plate (slab roll back). The trench retreat in turn causes extension, thinning, and incipient rifting of the upper lithosphere (including the magmatic arc) and associated magmatism (Brévenne; 360 Ma). The partially molten portion of the subducted lithosphere then flows towards the spreading centre and emplaces at crustal depths c. 355–350 Ma. LGU, Lower Gneiss Unit; UGU, Upper Gneiss Unit. [Colour figure can be viewed at wileyonlinelibrary.com]

represent the arc region and the Brévenne the transition to the back-arc region. The similarity between the age of the volcanic rocks and the eclogite facies metamorphism suggests that the eclogites belonged to this south-dipping slab during the Devonian. However, eclogites exposed in the FMC are commonly inferred to originate from a northward subducting slab (e.g., Faure et al., 2009; Lardeaux, 2014; Matte & Burg, 1981; Vanderhaeghe et al., 2020). This questions the polarity of the subduction.

The continental collision model for the FMC was built in reference to the Himalayas (Matte, 1986). It assumes the development of the crustal wedge to be related with a crust–mantle décollement developed in response to a strong slab pull (e.g., Mattauer, 1986). The inversion of the isograds considered as the hallmark of crustal-scale thrusts would—as in the Himalayas—require the thrust to be synthetic with the previous subduction (e.g., Le Fort, 1975). Considering the LAC as a major suture zone (Matte & Burg, 1981) and the south-vergent superposition of the UGU over the LGU, where an inverted medium-pressure gradient is developed (Briand, 1978; Burg et al., 1984), the subduction was inferred to be dipping to the north. In this case, the eclogites were exhumed in the forearc position (e.g., Vanderhaeghe et al., 2020). This model, however, is in contradiction with the results of detrital-zircon studies, which show that all the units in the FMC have Gondwanan affinity (e.g., Chelle-Michou et al., 2017), and the distribution of trilobite fauna across Western Europe (Ballèvre, 2016), which indicates the closing of a major oceanic domain to the north of, rather than within, the FMC. This precludes the interpretation of the eclogite-

15251314, 0, Downloaded from https://onlinelibrary.wiley.com/doi/10.1111/jmg.12733 by Cochrane France, Wiley Online Library on [03/06/2023]. See the Terms and Conditions (https://onlinelibrary.wiley.com/terms-and-conditions) on Wiley Online Library for rules of use; OA articles are governed by the applicable Creative Commons License

bearing LAC as a major suture zone. From this perspective, the lithological and geochemical zoning of the Morvan–Brévenne area suggesting a southward subduction may be regarded as carrying a first-order message. The suture zone situated to the north of the FMC (e.g., Ballèvre et al., 2009; Baptiste et al., 2016; Schulmann et al., 2022) would result from a late Devonian subduction dipping to the south (e.g., Faure et al., 1997; Pin et al., 1982), which promoted the development of the arc and back-arc domains in the Brévenne and Morvan areas (Pin & Paquette, 2002). The Devono–Carboniferous age of the eclogites determined here suits within the proposed timing of a north-lying, south-dipping subduction. In this hypothesis, the eclogites, which appear today to the south of the arc, are situated in a back-arc position. A similar situation is described in the Bohemian Massif (see after). By comparison, the LAC and the UGU would represent a piece of the northern Gondwana margin teared from the continent and eventually dragged into the subduction zone. Following the detachment of the crust from the subducting lithospheric mantle, this buoyant partially melted material would accumulate below the upper plate (i.e., relamination; cf. Hacker et al., 2011) and flow at the rear of the magmatic arc to the present-day location. Partial melting of the subducted material enhanced lateral migration and promoted the exhumation in the back-arc domain undergoing active rifting in the Devonian (Pin & Paquette, 1997). In this model, it is considered that thrusting of the UGU over the LGU is the result of the inversion of the back-arc basin and that the UGU and the LAC represent a portion of the relaminated material pinched between the margins of the closed back-arc domain—namely, the Morvan–Brévenne and LGU.

From the perspective of this model invoking a southward subduction and subsequent southward migration of the partially exhumed material, it is interesting to note that a similar southward flow of migmatite-hosted eclogites has been proposed in the southernmost part of the FMC, between the Lévézou and the Montagne Noire

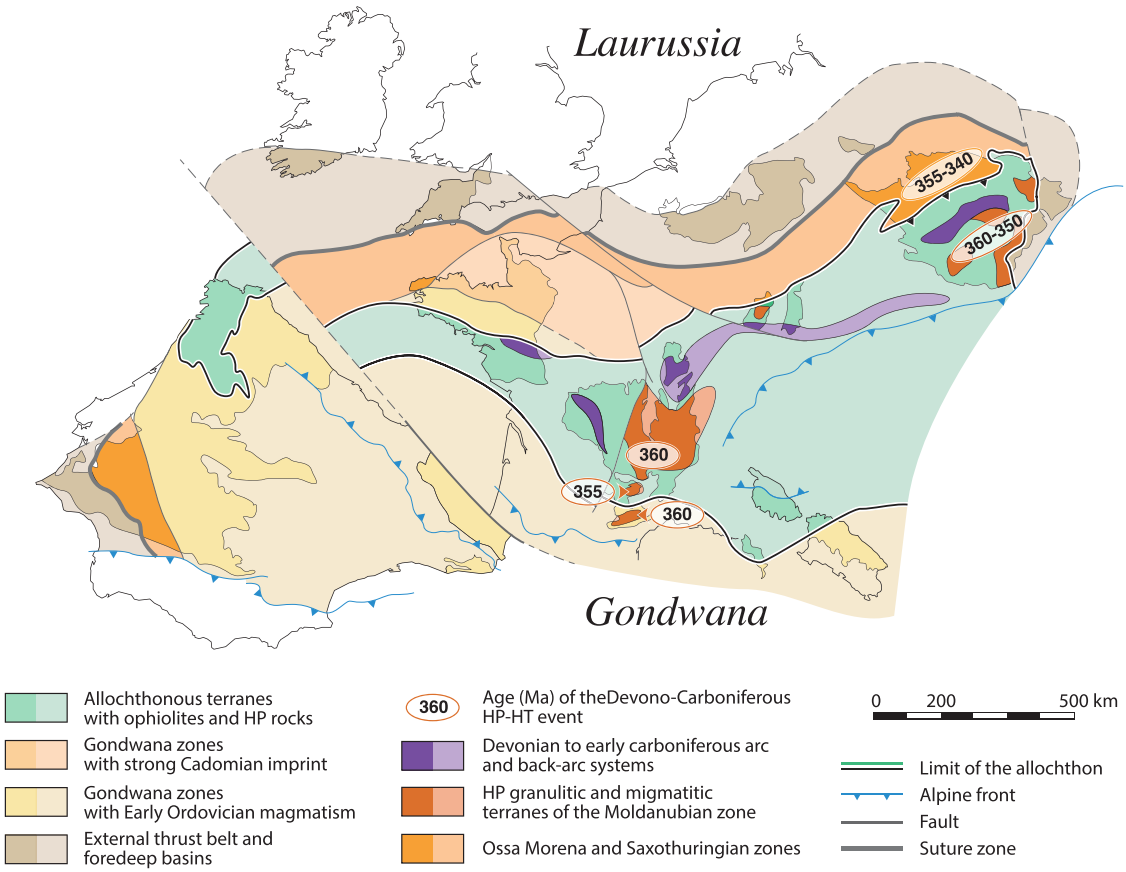

FIGURE 14 Sketch of the main Variscan massifs and terranes of the European Variscan orogen (modified after Martínez Catalán et al., 2007, 2021, and Schulmann et al., 2022) highlighting the possible correlations between the eastern French Massif Central and the Bohemian Massif based on the occurrence and age of the Devono–Carboniferous HP-HT rocks and the location of the associated arc and back-arc systems. Differences between the correlations before and after the present contribution can be seen by comparison with Figure 1a. [Colour figure can be viewed at wileyonlinelibrary.com]

15251314, 0, Downloaded from https://onlinelibrary.wiley.com/doi/10.1111/jmg.12733 by Cochrane France, Wiley Online Library on [03/06/2023]. See the Terms and Conditions (https://onlinelibrary.wiley.com/terms-and-conditions) on Wiley Online Library for rules of use; OA articles are governed by the applicable Creative Commons License

massifs (Pitra et al., 2022). This crustal flow is remarkably correlated with the progressive migration of the magmatism during the comparable 350–310 Ma time interval (Laurent et al., 2017).

11.2 | Implications for orogen-scale correlations

Although several correlations between the Variscan massifs exposed in western Europe have been proposed recently (e.g., Ballèvre et al., 2014; Lardeaux et al., 2014; Martínez Catalán et al., 2020), modern orogen-scale correlations stumbled on the Silurian age previously inferred for the Variscan subduction in the FMC. Using these data, Martínez Catalán et al. (2021) proposed that the FMC was a part of the so-called Mid-Variscan Allochthon, a nappe stack, where the units with the oldest high-pressure metamorphic age (c. 400 Ma) reached the highest metamorphic grade (Figure S11). However, our new data combined with a summary of modern *P–T* and radiometric data show that in the FMC, the eclogites that underwent the highest-grade conditions are the youngest (Figure S12). Hence, the FMC does not fit into the framework of the Mid-Variscan Allochthon but rather compares with some of the high-pressure rocks exposed in the Bohemian Massif (Figure 14). There, (U)HP granulitic complexes (e.g., Medaris et al., 2006; O'Brien & Carswell, 1993) occur several hundreds of kilometres away from the plate interface (e.g., Schulmann et al., 2009). Counterintuitively, the lower crust underlying the region between the suture zone and the granulitic complexes is characterized by low densities suggesting a felsic composition (Guy et al., 2011). Consequently, the crustal material in the (U)HP complexes is regarded as molten pieces of the subducted (Saxothuringian) continental crust detached from the downgoing slab, having laterally flowed behind the arc and having been relaminated to and exhumed in the core of the upper (Moldanubian) plate (Maierová et al., 2018, 2021; Nahodilová et al., 2020; Schulmann et al., 2014). The position of the studied eclogites at the rear of the arc in the FMC reminds the location of the (U)HP granulitic complexes of the Bohemian Massif, providing a more consistent picture of the Variscan orogen.

12 | CONCLUSIONS

The main conclusions of this study are as follows:

1. Eclogites from the Haut-Allier (northern Massif Central) record an Ordovician (c. 490 Ma) rifting event, a Devonian (c. 370–360 Ma) subduction, and a Carboniferous (c. 350 Ma) exhumation, followed by a late interaction (c. 310 Ma or later) with alkaline fluids. This study brings compelling evidence against the Silurian age previously proposed for the subduction.
2. Metamorphic zircon with clear eclogitic REE patterns (no Eu anomaly and flat HREE) and inclusions (garnet, rutile, and probably omphacite) shows concordant apparent ages that spread from c. 380 down to c. 310 Ma. Apparent ages younger than the cooling age of apatite (c. 350 Ma) unequivocally testify that zircon can recrystallize outside the conditions of the eclogite facies and reset its U–Pb system but preserve an apparent eclogitic signature. It is suggested that interaction with alkaline fluids at relatively low temperatures would lead to the recrystallization of zircon while leaving apatite unaffected.
3. The age of the eclogite facies metamorphism (c. 370–360 Ma) compares with that of the suprasubductional calc-alkaline Devonian volcanism in the northern Massif Central. Active thinning of the arc domain during the exhumation of the eclogites was likely driven by the roll back of the subducting lithospheric slab. The lithological and geochemical zoning of the volcanic rocks is consistent with a southward polarity of the subduction, at variance with the commonly accepted northward subduction of the so-called Massif Central Ocean. The present-day location of the eclogites suggests that they were exhumed at the rear of that arc after this southward subduction. The age and the architecture of the system question the existence of a major suture zone in the Massif Central and point to similarities with the geodynamics of the Bohemian Massif.

ACKNOWLEDGEMENTS

This work beneficiated the support of the French Geological Survey (BRGM) as well as an internal Czech Geological Survey grant (#311190), accorded to L. de Hoÿm de Marien. X. Le Coz is acknowledged for the production of the thin sections and Y. Lepagnot for the mineral separation. We are grateful for the assistance in SEM observations and EDS analyses of the staff of the CMEBA facility (ScanMAT, University of Rennes), which received financial support from the Région Bretagne and the European Union (CPER-FEDER 2007-2014). We are also grateful to J. Langlade and F. Schiavi, for their assistance during the EPMA analyses (Microsonde Ouest, IFRMER, Brest-Plouzané, France) and Raman spectroscopy analyses (Laboratoire Magmas et Volcans, Clermont-Ferrand, France), respectively. Jean-Marc Hénot is acknowledged for his help during the acquisition of SEM-CL images of zircons in thin sections (Laboratoire Magmas et Volcans,

15251314, 0, Downloaded from https://onlinelibrary.wiley.com/doi/10.1111/jmg.12733 by Cochrane France, Wiley Online Library on [03/06/2023]. See the Terms and Conditions (https://onlinelibrary.wiley.com/terms-and-conditions) on Wiley Online Library for rules of use; OA articles are governed by the applicable Creative Commons License

Clermont-Ferrand). Additional SEM observations were performed at the Faculty of Science, Charles University in Prague, with the help of M. Racek. L. de Hoÿm de Marien also thanks K. Schulmann, S. Collett, and A. Guy for exciting discussions about the correlation across the Variscan belt and guidance in the discovery of the geology of the Bohemian Massif. The paper benefited from the comments of two anonymous reviewers.

CONFLICT OF INTEREST STATEMENT

None of the authors have a conflict of interest to disclose.

ORCID

Luc de Hoÿm de Marien https://orcid.org/0000-0001-8216-6888
Pavel Pitra https://orcid.org/0000-0002-0462-2742
Marc Poujol https://orcid.org/0000-0001-8682-2926
Nathan Cogné https://orcid.org/0000-0002-7065-1373
Benjamin Le Bayon https://orcid.org/0000-0003-1807-166X

REFERENCES

Antignano, A., & Manning, C. E. (2008). Fluorapatite solubility in H_2O and H_2O–NaCl at 700 to 900°C and 0.7 to 2.0 GPa. *Chemical Geology*, *251*(1-4), 112–119. https://doi.org/10.1016/j.chemgeo.2008.03.001

Axelsson, E., Pape, J., Berndt, J., Corfu, F., Mezger, K., & Raith, M. M. (2018). Rutile R632—A new natural reference material for U-Pb and Zr determination. *Geostandards and Geoanalytical Research*, *42*(3), 319–338. https://doi.org/10.1111/ggr.12213

Ayers, J. C., DeLaCruz, K., Miller, C., & Switzer, O. (2003). Experimental study of zircon coarsening in quartzite $\pm H_2O$ at 1.0 GPa and 1000 °C, with implications for geochronological studies of high-grade metamorphism. *American Mineralogist*, *88*(2–3), 365–376. https://doi.org/10.2138/am-2003-2-313

Ballèvre, M. (2016). Provinces fauniques et domaines continentaux à l'Ordovicien. *Fossiles, HS*, *7*, 78–87.

Ballèvre, M., Bosse, V., Ducassou, C., & Pitra, P. (2009). Palaeozoic history of the Armorican Massif: Models for the tectonic evolution of the suture zones. *Comptes Rendus Geoscience*, *341*(2), 174–201. https://doi.org/10.1016/j.crte.2008.11.009

Ballèvre, M., Catalán, J. R. M., López-Carmona, A., Pitra, P., Abati, J., Fernández, R. D., Ducassou, C., Arenas, R., Bosse, V., Castiñeiras, P., Fernández-Suárez, J., Barreiro, J. G., Paquette, J.-L., Peucat, J.-J., Poujol, M., Ruffet, G., & Martínez, S. S. (2014). Correlation of the nappe stack in the Ibero-Armorican arc across the Bay of Biscay: A joint French–Spanish project. *Geological Society, London, Special Publications*, *405*(1), 77–113. https://doi.org/10.1144/SP405.13

Ballèvre, M., Fourcade, S., Capdevila, R., Peucat, J.-J., Cocherie, A., & Fanning, C. M. (2012). Geochronology and geochemistry of Ordovician felsic volcanism in the Southern Armorican Massif (Variscan belt, France): Implications for the breakup of Gondwana. *Gondwana Research*, *21*(4), 1019–1036. https://doi.org/10.1016/j.gr.2011.07.030

Baptiste, J., Martelet, G., Faure, M., Beccaletto, L., Reninger, P.-A., Perrin, J., & Chen, Y. (2016). Mapping of a buried basement combining aeromagnetic, gravity and petrophysical data: The substratum of Southwest Paris Basin, France. *Tectonophysics*, *683*, 333–348. https://doi.org/10.1016/j.tecto.2016.05.049

Barbey, P., Villaros, A., Marignac, C., & Montel, J.-M. (2015). Multiphase melting, magma emplacement and P-T-time path in late-collisional context: The Velay example (Massif Central, France). *Bulletin de la Société Géologique de France*, *186*(2–3), 93–116. https://doi.org/10.2113/gssgfbull.186.2-3.93

Beckman, V., & Möller, C. (2018). Prograde metamorphic zircon formation in gabbroic rocks: The tale of microtextures. *Journal of Metamorphic Geology*, *36*(9), 1221–1236. https://doi.org/10.1111/jmg.12443

Benmammar, A., Berger, J., Triantafyllou, A., Duchene, S., Bendaoud, A., Baele, J.-M., Bruguier, O., & Diot, H. (2020). Pressure-temperature conditions and significance of Upper Devonian eclogite and amphibolite facies metamorphisms in southern French Massif Central. *Bulletin de la Société Géologique de France*, *191*(1), 28. https://doi.org/10.1051/bsgf/2020033

Berger, J., Féménias, O., Ohnenstetter, D., Bruguier, O., Plissart, G., Mercier, J.-C. C., & Demaiffe, D. (2010). New occurrence of UHP eclogites in Limousin (French Massif Central): Age, tectonic setting and fluid–rock interactions. *Lithos*, *118*(3–4), 365–382. https://doi.org/10.1016/j.lithos.2010.05.013

Bingen, B., Austrheim, H., & Whitehouse, M. (2001). Ilmenite as a source for zirconium during high-grade metamorphism? Textural evidence from the Caledonides of Western Norway and implications for zircon geochronology. *Journal of Petrology*, *42*(2), 355–375. https://doi.org/10.1093/petrology/42.2.355

Boynton, W. V. (1984). Chapter 3—Cosmochemistry of the rare earth elements: Meteorite studies. In P. Henderson (Ed.), *Rare earth element geochemistry, developments in geochemistry* (Vol. 2) (pp. 63–114). Elsevier. https://doi.org/10.1016/B978-0-444-42148-7.50008-3

Briand, B. (1978). Métamorphisme inverse et chevauchement de "type Himalayen" dans la série de la vallée du Lot (Massif central français). *Comptes Rendus. Académie Des Sciences*, *286*, 729–731.

Burg, J. P., Leyreloup, A., Marchand, J., & Matte, P. (1984). Inverted metamorphic zonation and large-scale thrusting in the Variscan Belt: An example in the French Massif Central. *Geological Society, London, Special Publications*, *14*(1), 47–61. https://doi.org/10.1144/GSL.SP.1984.014.01.05

Burg, J.-P., & Leyreloup, A. (1989). Métamorphisme granulitique de roches granitiques en Rouergue (Massif Central). *Comptes Rendus de l'Académie Des Sciences. Série 2, Mécanique, Physique, Chimie, Sciences de l'univers. Sciences de la Terre*, *309*(7), 719–725.

Cao, W., Gilotti, J. A., & Massonne, H.-J. (2020). Partial melting of zoisite eclogite from the Sanddal area, North-East Greenland Caledonides. *European Journal of Mineralogy*, *32*(4), 405–425. https://doi.org/10.5194/ejm-32-405-2020

Chamberlain, K. R., & Bowring, S. A. (2001). Apatite–feldspar U–Pb thermochronometer: A reliable, mid-range (~450°C), diffusion-controlled system. *Chemical Geology*, *172*(1), 173–200. https://doi.org/10.1016/S0009-2541(00)00242-4

Chelle-Michou, C., Laurent, O., Moyen, J. F., Block, S., Paquette, J. L., Couzinié, S., Gardien, V., Vanderhaeghe, O.,

15251314, 0, Downloaded from https://onlinelibrary.wiley.com/doi/10.1111/jmg.12733 by Cochrane France, Wiley Online Library on [03/06/2023]. See the Terms and Conditions (https://onlinelibrary.wiley.com/terms-and-conditions) on Wiley Online Library for rules of use; OA articles are governed by the applicable Creative Commons License

Villaros, A., & Zeh, A. (2017). Pre-Cadomian to late-Variscan odyssey of the eastern Massif Central, France: Formation of the West European crust in a nutshell. *Gondwana Research*, *46*(Supplement C), 170–190. https://doi.org/10.1016/j.gr.2017.02.010

Chen, W. T., & Zhou, M.-F. (2017). Hydrothermal alteration of magmatic zircon related to NaCl-rich brines: Diffusion-reaction and dissolution-reprecipitation processes. *American Journal of Science*, *317*(2), 177–215. https://doi.org/10.2475/02.2017.02

Cherniak, D. J. (2000). Pb diffusion in rutile. *Contributions to Mineralogy and Petrology*, *139*(2), 198–207. https://doi.org/10.1007/PL00007671

Cherniak, D. J., & Watson, E. B. (2001). Pb diffusion in zircon. *Chemical Geology*, *172*(1), 5–24. https://doi.org/10.1016/S0009-2541(00)00233-3

Cherniak, D. J., Lanford, W. A., & Ryerson, F. J. (1991). Lead diffusion in apatite and zircon using ion implantation and Rutherford backscattering techniques. *Geochimica et Cosmochimica Acta*, *55*(6), 1663–1673. https://doi.org/10.1016/0016-7037(91)90137-T

Cochrane, R., Spikings, R. A., Chew, D., Wotzlaw, J.-F., Chiaradia, M., Tyrrell, S., Schaltegger, U., & Van der Lelij, R. (2014). High temperature (>350°C) thermochronology and mechanisms of Pb loss in apatite. *Geochimica et Cosmochimica Acta*, *127*, 39–56. https://doi.org/10.1016/j.gca.2013.11.028

Corfu, F., Hanchar, J. M., Hoskin, P. W. O., & Kinny, P. (2003). Atlas of zircon textures. *Reviews in Mineralogy and Geochemistry*, *53*(1), 469–500. https://doi.org/10.2113/0530469

Couzinié, S., Laurent, O., Chelle-Michou, C., Bouilhol, P., Paquette, J.-L., Gannoun, A.-M., & Moyen, J.-F. (2019). Detrital zircon U–Pb–Hf systematics of Ediacaran metasediments from the French Massif Central: Consequences for the crustal evolution of the north Gondwana margin. *Precambrian Research*, *324*, 269–284. https://doi.org/10.1016/j.precamres.2019.01.016

Couzinié, S., Laurent, O., Poujol, M., Mintrone, M., Chelle-Michou, C., Moyen, J. F., Bouilhol, P., Vezinet, A., & Marko, L. (2017). Cadomian S-type granites as basement rocks of the Variscan belt (Massif Central, France): Implications for the crustal evolution of the north Gondwana margin. *Lithos*, *286*(Supplement C), 16–34. https://doi.org/10.1016/j.lithos.2017.06.001

Couzinié, S., Moyen, J. F., Villaros, A., Paquette, J. L., Scarrow, J. H., & Marignac, C. (2014). Temporal relationships between Mg-K mafic magmatism and catastrophic melting of the Variscan crust in the southern part of Velay Complex (Massif Central, France). *Journal of Geosciences*, *59*, 1–18. https://doi.org/10.3190/jgeosci.155

de Hoÿm de Marien, L., Pitra, P., Cagnard, F., & le Bayon, B. (2020). Prograde and retrograde *P–T* evolution of a Variscan high-temperature eclogite, French Massif Central, Haut-Allier. *BSGF - Earth Sciences Bulletin*, *191*, 14. https://doi.org/10.1051/bsgf/2020016

Delfour, J. (1989). Données lithostratigraphiques et géochimiques sur le Dévono-Dinantien de la partie sud du faisceau du Morvan (nord-est du Massif central français). *Géologie de la France*, *4*, 49–77.

Ducrot, J., Lancelot, J. R., & Marchand, J. (1983). Datation U-Pb sur zircons de l'éclogite de La Borie (Haut-Allier, France) et conséquences sur l'évolution ante-hercynienne de l'Europe occidentale. *Earth and Planetary Science Letters*, *62*(3), 385–394. https://doi.org/10.1016/0012-821X(83)90009-2

Ernst, W. G., & Liou, J. G. (2008). High- and ultrahigh-pressure metamorphism: Past results and future prospects. *American Mineralogist*, *93*(11–12), 1771–1786. https://doi.org/10.2138/am.2008.2940

Faure, M., Charonnat, X., & Chauvet, A. (1999). Schéma structural et évolution tectonique du domaine para-autochtone cévenol de la chaîne hercynienne (Massif central français). *Comptes Rendus de l'Académie des Sciences - Series IIA - Earth and Planetary Science*, *328*(6), 401–407. https://doi.org/10.1016/S1251-8050(99)80106-2

Faure, M., Lardeaux, J. M., & Ledru, P. (2009). A review of the pre-Permian geology of the Variscan French Massif Central. *Comptes Rendus Geoscience*, *341*(2), 202–213. https://doi.org/10.1016/j.crte.2008.12.001

Faure, M., Leloix, C., & Roig, J. Y. (1997). L'Evolution polycyclique de la chaine hercynienne. *Bulletin de la Société Géologique de France*, *168*(6), 695–705.

Ferrero, S., Bartoli, O., Cesare, B., Salvioli-Mariani, E., Acosta-Vigil, A., Cavallo, A., Groppo, C., & Battiston, S. (2012). Microstructures of melt inclusions in anatectic metasedimentary rocks. *Journal of Metamorphic Geology*, *30*(3), 303–322. https://doi.org/10.1111/j.1525-1314.2011.00968.x

Forestier, F. H., Lasnier, B., Leyreloup, A., & Marchand, J. (1973). Vues nouvelles sur la catazone dans le Massif Central francais et le Massif Armoricain, de l'affleurement au Moho. *Bulletin de la Société Géologique de France*, *S7-XV*(5–6), 562–578. https://doi.org/10.2113/gssgfbull.S7-XV.5-6.562

Forestier, F.-H. (1961). Métamorphisme hercynien et antéhercynien dans le bassin du haut-Allier (Massif Central français). PhD Thesis, Université de Clermont-Ferrand. https://tel.archives-ouvertes.fr/tel-00765853

Gardien, V., Lardeaux, J.-M., & Misseri, M. (1988). Les péridotites des Monts du Lyonnais (M.C.F.): Témoins privilégiés d'une subduction de lithosphère paléozoïque. *Comptes Rendus de l'Académie Des Sciences. Série 2, Mécanique, Physique, Chimie, Sciences de l'univers, Sciences de la Terre*, *307*(19), 1967–1972.

Gardien, V., Tegyey, M., Lardeaux, J. M., Misseri, M., & Dufour, E. (1990). Crust-mantle relationships in the French Variscan chain: The example of the Southern Monts du Lyonnais unit (eastern French Massif Central). *Journal of Metamorphic Geology*, *8*(5), 477–492. https://doi.org/10.1111/j.1525-1314.1990.tb00481.x

Gardien, V., Vanderhaeghe, O., Arnaud, N., Cocherie, A., Grange, M., & Lécuyer, C. (2011). Thermal maturation and exhumation of a middle orogenic crust in the Livradois area (French Massif Central). *Bulletin de la Société Géologique de France*, *182*(1), 5–24. https://doi.org/10.2113/gssgfbull.182.1.5

Geisler, T., Schaltegger, U., & Tomaschek, F. (2007). Re-equilibration of zircon in aqueous fluids and melts. *Elements*, *3*(1), 43–50. https://doi.org/10.2113/gselements.3.1.43

Giraud, A., Marchand, J., Dupuy, C., & Dostal, J. (1984). Geochemistry of leptyno-amphibolite complex from Haut Allier (French Massif Central). *Lithos*, *17*, 203–214. https://doi.org/10.1016/0024-4937(84)90020-3

15251314, 0, Downloaded from https://onlinelibrary.wiley.com/doi/10.1111/jmg.12733 by Cochrane France, Wiley Online Library on [03/06/2023]. See the Terms and Conditions (https://onlinelibrary.wiley.com/terms-and-conditions) on Wiley Online Library for rules of use; OA articles are governed by the applicable Creative Commons License

Godard, G. (1990). Découverte d'éclogites, de péridotites à spinelle et d'amphibolites à anorthite, spinelle et corindon dans le Morvan. *Comptes Rendus de l'Académie Des Sciences*, *310*(3), 227–232.

Godard, G. (2001). Eclogites and their geodynamic interpretation: A history. *Journal of Geodynamics*, *32*(1), 165–203. https://doi.org/10.1016/S0264-3707(01)00020-5

Guy, A., Edel, J.-B., Schulmann, K., Tomek, Č., & Lexa, O. (2011). A geophysical model of the Variscan orogenic root (Bohemian Massif): Implications for modern collisional orogens. *Lithos*, *124*(1–2), 144–157. https://doi.org/10.1016/j.lithos.2010.08.008

Hacker, B. R., Kelemen, P. B., & Behn, M. D. (2011). Differentiation of the continental crust by relamination. *Earth and Planetary Science Letters*, *307*(3), 501–516. https://doi.org/10.1016/j.epsl.2011.05.024

Harley, S. L., Kelly, N. M., & Möller, A. (2007). Zircon behaviour and the thermal histories of mountain chains. *Elements*, *3*(1), 25–30. https://doi.org/10.2113/gselements.3.1.25

Harlov, D. E. (2015). Apatite: A fingerprint for metasomatic processes. *Elements*, *11*(3), 171–176. https://doi.org/10.2113/gselements.11.3.171

Harlov, D. E., Andersson, U. B., Förster, H.-J., Nyström, J. O., Dulski, P., & Broman, C. (2002). Apatite–monazite relations in the Kiirunavaara magnetite–apatite ore, northern Sweden. *Chemical Geology*, *191*(1), 47–72. https://doi.org/10.1016/S0009-2541(02)00148-1

Harrison, T. M., Catlos, E. J., & Montel, J.-M. (2002). U-Th-Pb dating of phosphate minerals. *Reviews in Mineralogy and Geochemistry*, *48*(1), 524–558. https://doi.org/10.2138/rmg.2002.48.14

Hofmann, A. E., Baker, M. B., & Eiler, J. M. (2014). Sub-micron-scale trace-element distributions in natural zircons of known provenance: Implications for Ti-in-zircon thermometry. *Contributions to Mineralogy and Petrology*, *168*(3), 1057. https://doi.org/10.1007/s00410-014-1057-8

Holness, M. B., & Sawyer, E. W. (2008). On the pseudomorphing of melt-filled pores during the crystallization of migmatites. *Journal of Petrology*, *49*(7), 1343–1363. https://doi.org/10.1093/petrology/egn028

Holness, M. B., Cesare, B., & Sawyer, E. W. (2011). Melted rocks under the microscope: Microstructures and their interpretation. *Elements*, *7*(4), 247–252. https://doi.org/10.2113/gselements.7.4.247

Horstwood, M. S. A., Košler, J., Gehrels, G., Jackson, S. E., McLean, N. M., Paton, C., Pearson, N. J., Sircombe, K., Sylvester, P., Vermeesch, P., Bowring, J. F., Condon, D. J., & Schoene, B. (2016). Community-derived standards for LA-ICP-MS U-(Th-)Pb geochronology—Uncertainty propagation, age interpretation and data reporting. *Geostandards and Geoanalytical Research*, *40*(3), 311–332. https://doi.org/10.1111/j.1751-908X.2016.00379.x

Hoskin, P. W. O., & Black, L. P. (2000). Metamorphic zircon formation by solid-state recrystallization of protolith igneous zircon. *Journal of Metamorphic Geology*, *18*(4), 423–439. https://doi.org/10.1046/j.1525-1314.2000.00266.x

Jackson, S. E., Pearson, N. J., Griffin, W. L., & Belousova, E. A. (2004). The application of laser ablation-inductively coupled plasma-mass spectrometry to in situ U–Pb zircon geochronology. *Chemical Geology*, *211*(1), 47–69. https://doi.org/10.1016/j.chemgeo.2004.06.017

Janoušek, V., Farrow, C. M., & Erban, V. (2006). Interpretation of whole-rock geochemical data in igneous geochemistry: Introducing geochemical data toolkit (GCDkit). *Journal of Petrology*, *47*(6), 1255–1259. https://doi.org/10.1093/petrology/egl013

Kelsey, D. E., Clark, C., & Hand, M. (2008). Thermobarometric modelling of zircon and monazite growth in melt-bearing systems: Examples using model metapelitic and metapsammitic granulites. *Journal of Metamorphic Geology*, *26*(2), 199–212. https://doi.org/10.1111/j.1525-1314.2007.00757.x

Kent, A. J. R., Jacobsen, B., Peate, D. W., Waight, T. E., & Baker, J. A. (2004). Isotope dilution MC-ICP-MS rare earth element analysis of geochemical reference materials NIST SRM 610, NIST SRM 612, NIST SRM 614, BHVO-2G, BHVO-2, BCR-2G, JB-2, WS-E, W-2, AGV-1 and AGV-2. *Geostandards and Geoanalytical Research*, *28*(3), 417–429. https://doi.org/10.1111/j.1751-908X.2004.tb00760.x

Klimm, K., Blundy, J. D., & Green, T. H. (2008). Trace element partitioning and accessory phase saturation during H_2O-saturated melting of basalt with implications for subduction zone chemical fluxes. *Journal of Petrology*, *49*(3), 523–553. https://doi.org/10.1093/petrology/egn001

Kohn, M. J., Corrie, S. L., & Markley, C. (2015). The fall and rise of metamorphic zircon. *American Mineralogist*, *100*(4), 897–908. https://doi.org/10.2138/am-2015-5064

Košler, J., Bowes, D. R., & Konopásek, J. M. (2004). Laser ablation ICPMS dating of zircons in Erzgebirge orthogneisses: Evidence for Early Cambrian and Early Ordovician granitic plutonism in the western Bohemian Massif. *European Journal of Mineralogy*, *16*, 15–22. https://doi.org/10.1127/0935-1221/2004/0016-0015

Kramers, J., Frei, R., Newville, M., Kober, B., & Villa, I. (2009). On the valency state of radiogenic lead in zircon and its consequences. *Chemical Geology*, *261*(1), 4–11. https://doi.org/10.1016/j.chemgeo.2008.09.010

Kroner, U., & Romer, R. L. (2013). Two plates—Many subduction zones: The Variscan orogeny reconsidered. *Gondwana Research*, *24*(1), 298–329. https://doi.org/10.1016/j.gr.2013.03.001

Labrousse, L., Prouteau, G., & Ganzhorn, A.-C. (2011). Continental exhumation triggered by partial melting at ultrahigh pressure. *Geology*, *39*(12), 1171–1174. https://doi.org/10.1130/G32316.1

Lang, H. M., & Gilotti, J. A. (2007). Partial melting of metapelites at ultrahigh-pressure conditions, Greenland Caledonides. *Journal of Metamorphic Geology*, *25*(2), 129–147. https://doi.org/10.1111/j.1525-1314.2006.00687.x

Lardeaux, J. M. (2014). Deciphering orogeny: A metamorphic perspective examples from European Alpine and Variscan belts. *Bulletin de la Société Géologique de France*, *185*(5), 281–310. https://doi.org/10.2113/gssgfbull.185.5.281

Lardeaux, J. M., Ledru, P., Daniel, I., & Duchene, S. (2001). The Variscan French Massif Central—A new addition to the ultrahigh pressure metamorphic 'club': Exhumation processes and geodynamic consequences. *Tectonophysics*, *332*(1–2), 143–167. https://doi.org/10.1016/S0040-1951(00)00253-5

Lardeaux, J. M., Schulmann, K., Faure, M., Janoušek, V., Lexa, O., Skrzypek, E., Edel, J. B., & Štípská, P. (2014). The

15251314, 0, Downloaded from https://onlinelibrary.wiley.com/doi/10.1111/jmg.12733 by Cochrane France, Wiley Online Library on [03/06/2023]. See the Terms and Conditions (https://onlinelibrary.wiley.com/terms-and-conditions) on Wiley Online Library for rules of use; OA articles are governed by the applicable Creative Commons License

Moldanubian Zone in the French Massif Central, Vosges/Schwarzwald and Bohemian Massif revisited: Differences and similarities. *Geological Society, London, Special Publications*, *405*(1), 7–44. https://doi.org/10.1144/SP405.14

Lasnier, B. (1968). Découverte de roches éclogitiques dans le groupe leptyno-amphibolique des Monts du Lyonnais (Massif Central français). *Bulletin de la Société Géologique de France*, *S7-X*(2), 179–185. https://doi.org/10.2113/gssgfbull.S7-X.2.179

Lasnier, B. (1971). Les péridotites et pyroxénolites à grenat du Bois des feuilles (Monts du lyonnais) (France). *Contributions to Mineralogy and Petrology*, *34*(1), 29–42. https://doi.org/10.1007/BF00376029

Lasnier, B. (1977). Persistance d'une série granulitique au coeur du Massif Central français, Haut-Allier: Les termes basiques, ultrabasiques et carbonatés. PhD thesis, Université de Nantes. https://tel.archives-ouvertes.fr/tel-01079965/document

Laurent, O., Couzinié, S., Zeh, A., Vanderhaeghe, O., Moyen, J. F., Villaros, A., Gardien, V., & Chelle-Michou, C. (2017). Protracted, coeval crust and mantle melting during Variscan late-orogenic evolution: U–Pb dating in the eastern French Massif Central. *International Journal of Earth Sciences*, *106*(2), 421–451. https://doi.org/10.1007/s00531-016-1434-9

Le Fort, P. (1975). Himalayas: The collided range. Present knowledge of the continental arc. *American Journal of Science*, *275*(1), 1–44.

Ledru, P., Lardeaux, J. M., Santallier, D., Autran, A., Quenardel, J. M., Floc'h, J. P., Lerouge, G., Maillet, N., Marchand, J., & Ploquin, A. (1989). Où sont les nappes dans le Massif central français ? *Bulletin de la Société Géologique de France*, *8*(3), 605–618. https://doi.org/10.2113/gssgfbull.V.3.605

Lee, J. K. W., Williams, I. S., & Ellis, D. J. (1997). Pb, U and Th diffusion in natural zircon. *Nature*, *390*, 159–162. https://doi.org/10.1038/36554

Leloix, C., Faure, M., & Feybesse, J.-L. (1999). Hercynian polyphase tectonics in the northeast French massif central: The closure of the Brévenne Devonian–Dinantian rift. *International Journal of Earth Sciences*, *88*(3), 409–421. https://doi.org/10.1007/s005310050275

Linnemann, U., Pereira, F., Jeffries, T. E., Drost, K., & Gerdes, A. (2008). The Cadomian Orogeny and the opening of the Rheic Ocean: The diacrony of geotectonic processes constrained by LA-ICP-MS U–Pb zircon dating (Ossa-Morena and Saxo-Thuringian Zones, Iberian and Bohemian Massifs). *Tectonophysics*, *461*(1), 21–43. https://doi.org/10.1016/j.tecto.2008.05.002

Lotout, C., Pitra, P., Poujol, M., & Driessche, J. V. D. (2017). Ordovician magmatism in the Lévézou massif (French Massif Central): Tectonic and geodynamic implications. *International Journal of Earth Sciences*, *106*(2), 501–515. https://doi.org/10.1007/s00531-016-1387-z

Lotout, C., Pitra, P., Poujol, M., Anczkiewicz, R., & Van Den Driessche, J. (2018). Timing and duration of Variscan high-pressure metamorphism in the French Massif Central: A multimethod geochronological study from the Najac Massif. *Lithos*, *308–309*, 381–394. https://doi.org/10.1016/j.lithos.2018.03.022

Lotout, C., Poujol, M., Pitra, P., Anczkiewicz, R., & Van Den Driessche, J. (2020). From burial to exhumation: Emplacement and metamorphism of mafic eclogitic terranes constrained through multimethod petrochronology: A case study from the Lévézou massif (French Massif Central, Variscan belt). *Journal of Petrology*, *61*, egaa046. https://doi.org/10.1093/petrology/egaa046

Luginbühl, S. M. (2015). Phase relations, compositions and trace element partitioning of solid and mobile phases in the hydrous MORB system at 2–3 GPa (190 p.) PhD thesis, ETH Zurich. https://doi.org/10.3929/ETHZ-A-010659285

Luvizotto, G. L., Zack, T., Meyer, H. P., Ludwig, T., Triebold, S., Kronz, A., Münker, C., Stockli, D. F., Prowatke, S., Klemme, S., Jacob, D. E., & von Eynatten, H. (2009). Rutile crystals as potential trace element and isotope mineral standards for microanalysis. *Chemical Geology*, *261*(3), 346–369. https://doi.org/10.1016/j.chemgeo.2008.04.012

Maierová, P., Schulmann, K., & Gerya, T. (2018). Relamination styles in collisional orogens. *Tectonics*, *37*(1), 224–250. https://doi.org/10.1002/2017TC004677

Maierová, P., Schulmann, K., Štípská, P., Gerya, T., & Lexa, O. (2021). Trans-lithospheric diapirism explains the presence of ultra-high pressure rocks in the European Variscides. *Communications Earth & Environment*, *2*(1), 56. https://doi.org/10.1038/s43247-021-00122-w

Marchand, J. (1974). Persistance d'une série granulitique au coeur du Massif Central français, Haut-Allier: Les termes acides. PhD thesis, Université de Nantes. https://hal.inria.fr/UNIV-NANTES-THESES/tel-01087737v1

Martin, L. A. J., Duchêne, S., Deloule, E., & Vanderhaeghe, O. (2008). Mobility of trace elements and oxygen in zircon during metamorphism: Consequences for geochemical tracing. *Earth and Planetary Science Letters*, *267*(1), 161–174. https://doi.org/10.1016/j.epsl.2007.11.029

Martínez Catalán, J. R., Arenas, R., García, F. D., Cuadra, P. G., Gómez Barreiro, J., Abati, J., Castiñeiras, P., Fernández-Suárez, J., Martínez, S. S., Andonaegui, P., Clavijo, E. G., Montes, A. D., Pascual, F. J. R., & Aguado, B. V. (2007). Space and time in the tectonic evolution of the northwestern Iberian Massif: Implications for the Variscan belt. In *Geological society of America memoirs* (Vol. 200, pp. 403–423). Geological Society of America. https://doi.org/10.1130/2007.1200(21)

Martínez Catalán, J. R., Collett, S., Schulmann, K., Aleksandrowski, P., & Mazur, S. (2020). Correlation of allochthonous terranes and major tectonostratigraphic domains between NW Iberia and the Bohemian Massif, European Variscan belt. *International Journal of Earth Sciences*, *109*, 1105–1131. https://doi.org/10.1007/s00531-019-01800-z

Martínez Catalán, J. R., Schulmann, K., & Ghienne, J.-F. (2021). The Mid-Variscan Allochthon: Keys from correlation, partial retrodeformation and plate-tectonic reconstruction to unlock the geometry of a non-cylindrical belt. *Earth-Science Reviews*, *220*, 103700. https://doi.org/10.1016/j.earscirev.2021.103700

Mattauer, M. (1986). Intracontinental subduction, crust-mantle décollement and crustal-stacking wedge in the Himalayas and other collision belts. *Geological Society, London, Special Publications*, *19*(1), 37–50. https://doi.org/10.1144/GSL.SP.1986.019.01.02

Matte, P. (1986). Tectonics and plate tectonics model for the Variscan belt of Europe. *Tectonophysics*, *126*(2), 329–374. https://doi.org/10.1016/0040-1951(86)90237-4

15251314, 0, Downloaded from https://onlinelibrary.wiley.com/doi/10.1111/jmg.12733 by Cochrane France, Wiley Online Library on [03/06/2023]. See the Terms and Conditions (https://onlinelibrary.wiley.com/terms-and-conditions) on Wiley Online Library for rules of use; OA articles are governed by the applicable Creative Commons License

Matte, P. (1991). Accretionary history and crustal evolution of the Variscan belt in Western Europe. *Tectonophysics*, *196*(3), 309–337. https://doi.org/10.1016/0040-1951(91)90328-P

Matte, P., & Burg, J. P. (1981). Sutures, thrusts and nappes in the Variscan arc of western Europe: Plate tectonic implications. *Geological Society, London, Special Publications*, *9*(1), 353–358. https://doi.org/10.1144/GSL.SP.1981.009.01.31

McDowell, F. W., McIntosh, W. C., & Farley, K. A. (2005). A precise ^{40}Ar–^{39}Ar reference age for the Durango apatite (U–Th)/He and fission-track dating standard. *Chemical Geology*, *214*(3), 249–263. https://doi.org/10.1016/j.chemgeo.2004.10.002

Medaris, L. G., Beard, B. L., & Jelínek, E. (2006). Mantle-derived, UHP garnet pyroxenite and eclogite in the Moldanubian Gföhl Nappe, Bohemian Massif: A geochemical review, new P-T determinations, and tectonic interpretation. *International Geology Review*, *48*(9), 765–777. https://doi.org/10.2747/0020-6814.48.9.765

Mercier, L., Johan, V., Lardeaux, J. M., & Ledru, P. (1989). Découverte d'éclogites dans l'Artense (M.C.F.) Implications pour la définiton des nappes à l'Est du Sillon Houiller. *Comptes Rendus de l'Académie Des Sciences*, *308*, 315–320.

Mercier, L., Lardeaux, J.-M., & Davy, P. (1991). On the tectonic significance of retrograde P-T-t paths in eclogites of the French Massif Central. *Tectonics*, *10*(1), 131–140. https://doi.org/10.1029/90TC02094

Miyashiro, A. (1961). Evolution of metamorphic belts. *Journal of Petrology*, *2*(3), 277–311. https://doi.org/10.1093/petrology/2.3.277

Miyashiro, A. (1972). Metamorphism and related magmatism in plate tectonics. *American Journal of Science*, *272*(7), 629–656. https://doi.org/10.2475/ajs.272.7.629

Moyen, J.-F., Laurent, O., Chelle-Michou, C., Couzinié, S., Vanderhaeghe, O., Zeh, A., Villaros, A., & Gardien, V. (2017). Collision vs. subduction-related magmatism: Two contrasting ways of granite formation and implications for crustal growth. *Lithos*, *277*(Supplement C), 154–177. https://doi.org/10.1016/j.lithos.2016.09.018

Nahodilová, R., Hasalová, P., Štípská, P., Schulmann, K., Závada, P., Míková, J., Kylander-Clark, A., & Maierová, P. (2020). Exhumation of subducted continental crust along the arc region. *Gondwana Research*, *80*, 157–187. https://doi.org/10.1016/j.gr.2019.10.011

Nance, R. D., & Linnemann, U. (2008). The Rheic Ocean: Origin, evolution, and significance. *GSA Today*, *18*(12), 4. https://doi.org/10.1130/GSATG24A.1

Nicollet, C. (1977). Une nouvelle éclogite à disthène et corindon primaires dans les complexes leptyno-amphiboliques du Massif central français (Lévezou, Rouergue). *Bulletin de Mineralogie*, *100*, 334–337.

Nicollet, C., & Leyreloup, A. (1978). Pétrologie des niveaux trondhjémitiques de haute pression associés aux éclogites et amphibolites des complexes leptyno-amphiboliques du Massif Central français. *Canadian Journal of Earth Sciences*, *15*(5), 696–707. https://doi.org/10.1139/e78-077

Nicollet, C., Lahlafi, M., & Lasnier, B. (1993). Occurence of a late Hercynian metamorphic event, of low pressure granulitic conditions, in the Haut-Allier (French Massif Central): Geodynamic implications. *Comptes Rendus de l'Academie des Sciences*, *317*, 1609–1615.

Nosenzo, F., Manzotti, P., Poujol, M., Ballèvre, M., & Langlade, J. (2022). A window into an older orogenic cycle: *P–T* conditions and timing of the pre-Alpine history of the Dora-Maira Massif (Western Alps). *Journal of Metamorphic Geology*, *40*(4), 789–821. https://doi.org/10.1111/jmg.12646

O'Brien, P. J., & Carswell, D. A. (1993). Tectonometamorphic evolution of the Bohemian Massif: Evidence from high pressure metamorphic rocks. *Geologische Rundschau*, *82*(3), 531–555. https://doi.org/10.1007/BF00212415

Palin, R. M., White, R. W., Green, E. C. R., Diener, J. F. A., Powell, R., & Holland, T. J. B. (2016). High-grade metamorphism and partial melting of basic and intermediate rocks. *Journal of Metamorphic Geology*, *34*(9), 871–892. https://doi.org/10.1111/jmg.12212

Paquette, J. L., Ballèvre, M., Peucat, J. J., & Cornen, G. (2017). From opening to subduction of an oceanic domain constrained by LA-ICP-MS U-Pb zircon dating (Variscan belt, Southern Armorican Massif, France). *Lithos*, *294-295*, 418–437. https://doi.org/10.1016/j.lithos.2017.10.005

Paquette, J. L., Monchoux, P., & Couturier, M. (1995). Geochemical and isotopic study of a norite-eclogite transition in the European Variscan belt: Implications for U/Pb zircon systematics in metabasic rocks. *Geochimica et Cosmochimica Acta*, *59*(8), 1611–1622. https://doi.org/10.1016/0016-7037(95)00067-A

Paquette, J.-L., Piro, J.-L., Devidal, J.-L., Bosse, V., Didier, A., Sanac, S., & Abdelnous, Y. (2014). Sensitivity enhancement in LA-ICP-MS by N2 addition to carrier gas: Application to radiometric dating of U-Th-bearing minerals. *Agilent ICP-MS Journal*, *58*, 1–5.

Paton, C., Hellstrom, J., Paul, B., Woodhead, J., & Hergt, J. (2011). Iolite: Freeware for the visualisation and processing of mass spectrometric data. *Journal of Analytical Atomic Spectrometry*, *26*(12), 2508–2518. https://doi.org/10.1039/C1JA10172B

Perchuk, A. L., Burchard, M., Maresch, W. V., & Schertl, H.-P. (2005). Fluid-mediated modification of garnet interiors under ultrahigh-pressure conditions. *Terra Nova*, *17*(6), 545–553. https://doi.org/10.1111/j.1365-3121.2005.00647.x

Perchuk, A. L., Burchard, M., Maresch, W. V., & Schertl, H.-P. (2008). Melting of hydrous and carbonate mineral inclusions in garnet host during ultrahigh pressure experiments. *Lithos*, *103*(1), 25–45. https://doi.org/10.1016/j.lithos.2007.09.008

Peterlongo, J. M. (1970). Pillow-lavas a bordure variolitique et matrice basique dans la serie metamorphique de la Brevenne (Rhone, Massif central francais). *Bulletin de la Société Géologique de France*, *S7-XII*(2), 190–194. https://doi.org/10.2113/gssgfbull.S7-XII.2.190

Peterlongo, J.-M. (1958). Les terrains crystallins des Monts du Lyonnais (Massif Central Français). PhD Thesis. Faculté des Sciences de l'Université de Clermont-Ferrand.

Pin, C., & Lancelot, J. (1982). U-Pb dating of an early paleozoic bimodal magmatism in the French Massif Central and of its further metamorphic evolution. *Contributions to Mineralogy and Petrology*, *79*(1), 1–12. https://doi.org/10.1007/BF00376956

Pin, C., & Marini, F. (1993). Early Ordovician continental break-up in Variscan Europe: Nd-Sr isotope and trace element evidence from bimodal igneous associations of the Southern Massif Central, France. *Lithos*, *29*(3), 177–196. https://doi.org/10.1016/0024-4937(93)90016-6

15251314, 0, Downloaded from https://onlinelibrary.wiley.com/doi/10.1111/jmg.12733 by Cochrane France, Wiley Online Library on [03/06/2023]. See the Terms and Conditions (https://onlinelibrary.wiley.com/terms-and-conditions) on Wiley Online Library for rules of use; OA articles are governed by the applicable Creative Commons License

Pin, C., & Paquette, J. L. (1997). A mantle-derived bimodal suite in the Hercynian Belt: Nd isotope and trace element evidence for a subduction-related rift origin of the Late Devonian Brévenne metavolcanics, Massif Central (France). *Contributions to Mineralogy and Petrology*, *129*(2–3), 222–238. https://doi.org/10.1007/s004100050334

Pin, C., & Paquette, J. L. (2002). Le magmatisme basique calcoalcalin d'âge dévono-dinantien du nord du Massif Central, témoin d'une marge active hercynienne: Arguments géochimiques et isotopiques Sr/Nd. *Geodinamica Acta*, *15*(1), 63–77. https://doi.org/10.1080/09853111.2002.10510739

Pin, C., & Vielzeuf, D. (1988). Les granulites de haute-pression d'Europe moyenne temoins d'une subduction eo-hercynienne; implications sur l'origine des groupes leptyno-amphiboliques. *Bulletin de la Société Géologique de France*, *IV*(1), 13–20. https://doi.org/10.2113/gssgfbull.IV.1.13

Pin, C., Dupuy, C., & Peterlongo, J.-M. (1982). Répartition des terres rares dans les roches volcaniques basiques dévono-dinantiennes du Nord-Est du Massif Central. *Bulletin de la Société Géologique de France*, *S7-XXIV*(4), 669–676. https://doi.org/10.2113/gssgfbull.S7-XXIV.4.669

Pitra, P., Poujol, M., Van Den Driessche, J., Bretagne, E., Lotout, C., & Cogné, N. (2022). Late Variscan (315 Ma) subduction or deceptive zircon REE patterns and U–Pb dates from migmatite-hosted eclogites? (Montagne Noire, France). *Journal of Metamorphic Geology*, *40*(1), 39–65. https://doi.org/10.1111/jmg.12609

Pochon, A., Poujol, M., Gloaguen, E., Branquet, Y., Cagnard, F., Gumiaux, C., & Gapais, D. (2016). U-Pb LA-ICP-MS dating of apatite in mafic rocks: Evidence for a major magmatic event at the Devonian-Carboniferous boundary in the Armorican Massif (France). *American Mineralogist*, *101*(11), 2430–2442. https://doi.org/10.2138/am-2016-5736

Poujol, M., Pitra, P., Van Den Driessche, J., Tartèse, R., Ruffet, G., Paquette, J. L., & Poilvet, J. C. (2016). Two-stage partial melting during the Variscan extensional tectonics (Montagne Noire, France). *International Journal of Earth Sciences*, *1–24*, 477–500. https://doi.org/10.1007/s00531-016-1369-1

Roger, F., Teyssier, C., Respaut, J.-P., Rey, P. F., Jolivet, M., Whitney, D. L., Paquette, J.-L., & Brunel, M. (2015). Timing of formation and exhumation of the Montagne Noire double dome, French Massif Central. *Tectonophysics*, *640–641*, 53–69. https://doi.org/10.1016/j.tecto.2014.12.002

Rubatto, D. (2002). Zircon trace element geochemistry: Partitioning with garnet and the link between U–Pb ages and metamorphism. *Chemical Geology*, *184*(1), 123–138. https://doi.org/10.1016/S0009-2541(01)00355-2

Rubatto, D. (2017). Zircon: The metamorphic mineral. *Reviews in Mineralogy and Geochemistry*, *83*(1), 261–295. https://doi.org/10.2138/rmg.2017.83.9

Rubatto, D., & Gebauer, D. (2000). Use of cathodoluminescence for U-Pb zircon dating by ion microprobe: Some examples from the Western Alps. In M. Pagel, V. Barbin, P. Blanc, & D. Ohnenstetter (Eds.), *Cathodoluminescence in geosciences* (pp. 373–400). Springer. https://doi.org/10.1007/978-3-662-04086-7_15

Rubatto, D., Müntener, O., Barnhoorn, A., & Gregory, C. (2008). Dissolution-reprecipitation of zircon at low-temperature, high-pressure conditions (Lanzo Massif, Italy). *American Mineralogist*, *93*(10), 1519–1529. https://doi.org/10.2138/am.2008.2874

Santallier, D., Briand, B., Menot, R. P., & Piboule, M. (1988). Les complexes leptyno-amphiboliques (CLA): Revue critique et suggestions pour un meilleur emploi de ce terme. *Bulletin de la société géologique de France*, *1*, 3–12. https://doi.org/10.2113/gssgfbull.IV.1.3

Schaltegger, U., Fanning, C. M., Günther, D., Maurin, J. C., Schulmann, K., & Gebauer, D. (1999). Growth, annealing and recrystallization of zircon and preservation of monazite in high-grade metamorphism: Conventional and in-situ U-Pb isotope, cathodoluminescence and microchemical evidence. *Contributions to Mineralogy and Petrology*, *134*(2), 186–201. https://doi.org/10.1007/s004100050478

Schmädicke, E., Will, T. M., Ling, X., Li, X.-H., & Li, Q.-L. (2018). Rare peak and ubiquitous post-peak zircon in eclogite: Constraints for the timing of UHP and HP metamorphism in Erzgebirge, Germany. *Lithos*, *322*, 250–267. https://doi.org/10.1016/j.lithos.2018.10.017

Schoene, B., & Bowring, S. A. (2006). U–Pb systematics of the McClure Mountain syenite: Thermochronological constraints on the age of the $^{40}Ar/^{39}Ar$ standard. *Contributions to Mineralogy and Petrology*, *151*, 615–630. https://doi.org/10.1007/s00410-006-0077-4

Schulmann, K., Edel, J.-B., Martínez Catalán, J. R., Mazur, S., Guy, A., Lardeaux, J.-M., Ayarza, P., & Palomeras, I. (2022). Tectonic evolution and global crustal architecture of the European Variscan belt constrained by geophysical data. *Earth-Science Reviews*, *234*, 104195. https://doi.org/10.1016/j.earscirev.2022.104195

Schulmann, K., Konopásek, J., Janoušek, V., Lexa, O., Lardeaux, J.-M., Edel, J.-B., Štípská, P., & Ulrich, S. (2009). An Andean type Palaeozoic convergence in the Bohemian Massif. *Comptes Rendus Géoscience*, *341*(2), 266–286. https://doi.org/10.1016/j.crte.2008.12.006

Schulmann, K., Lexa, O., Janoušek, V., Lardeaux, J. M., & Edel, J. B. (2014). Anatomy of a diffuse cryptic suture zone: An example from the Bohemian Massif, European Variscides. *Geology*, *42*(4), 275–278. https://doi.org/10.1130/G35290.1

Schulz, B. (2014). Early carboniferous P-T path from the upper gneiss unit of Haut-Allier (French Massif Central)—Reconstructed by geothermobarometry and EMP-Th-U-Pb monazite dating. *Journal of Geosciences*, *59*(4), 327–349. https://doi.org/10.3190/Jgeosci.178

Sláma, J., Košler, J., Condon, D. J., Crowley, J. L., Gerdes, A., Hanchar, J. M., Horstwood, M. S. A., Morris, G. A., Nasdala, L., Norberg, N., Schaltegger, U., Schoene, B., Tubrett, M. N., & Whitehouse, M. J. (2008). Plešovice zircon—A new natural reference material for U–Pb and Hf isotopic microanalysis. *Chemical Geology*, *249*(1), 1–35. https://doi.org/10.1016/j.chemgeo.2007.11.005

Soman, A., Geisler, T., Tomaschek, F., Grange, M., & Berndt, J. (2010). Alteration of crystalline zircon solid solutions: A case study on zircon from an alkaline pegmatite from Zomba-Malosa, Malawi. *Contributions to Mineralogy and Petrology*, *160*, 909–930. https://doi.org/10.1007/s00410-010-0514-2

Spandler, C., Hermann, J., & Rubatto, D. (2004). Exsolution of thortveitite, yttrialite, and xenotime during low-temperature recrystallization of zircon from New Caledonia, and their significance for trace element incorporation in zircon. *American*

15251314, 0, Downloaded from https://onlinelibrary.wiley.com/doi/10.1111/jmg.12733 by Cochrane France, Wiley Online Library on [03/06/2023]. See the Terms and Conditions (https://onlinelibrary.wiley.com/terms-and-conditions) on Wiley Online Library for rules of use; OA articles are governed by the applicable Creative Commons License

Mineralogist, *89*(11–12), 1795–1806. https://doi.org/10.2138/am-2004-11-1226

Stacey, J. S., & Kramers, J. D. (1975). Approximation of terrestrial lead isotope evolution by a two-stage model. *Earth and Planetary Science Letters*, *26*(2), 207–221. https://doi.org/10.1016/0012-821X(75)90088-6

Stampfli, G. M., Hochard, C., Vérard, C., Wilhem, C., & von Raumer, J. (2013). The formation of Pangea. *Tectonophysics*, *593*, 1–19. https://doi.org/10.1016/j.tecto.2013.02.037

Sun, S., & McDonough, W. F. (1989). Chemical and isotopic systematics of oceanic basalts: Implications for mantle composition and processes. *Geological Society, London, Special Publications*, *42*(1), 313–345. https://doi.org/10.1144/GSL.SP.1989.042.01.19

Sánchez-García, T., Bellido, F., & Quesada, C. (2003). Geodynamic setting and geochemical signatures of Cambrian–Ordovician rift-related igneous rocks (Ossa-Morena Zone, SW Iberia). *Tectonophysics*, *365*(1-4), 233–255. https://doi.org/10.1016/S0040-1951(03)00024-6

Štípská, P., Powell, R., Hacker, B. R., Holder, R., & Kylander-Clark, A. R. C. (2016). Uncoupled U/Pb and REE response in zircon during the transformation of eclogite to mafic and intermediate granulite (Blanský les, Bohemian Massif). *Journal of Metamorphic Geology*, *34*, 551–572. https://doi.org/10.1111/jmg.12193

Taylor, R. J. M., Clark, C., Fitzsimons, I. C. W., Santosh, M., Hand, M., Evans, N., & McDonald, B. (2014). Post-peak, fluid-mediated modification of granulite facies zircon and monazite in the Trivandrum Block, southern India. *Contributions to Mineralogy and Petrology*, *168*(2), 1044. https://doi.org/10.1007/s00410-014-1044-0

Thomson, S. N., Gehrels, G. E., Ruiz, J., & Buchwaldt, R. (2018). Routine low-damage apatite U-Pb dating using laser ablation–multicollector–ICPMS. *Geochemistry, Geophysics, Geosystems*, *13*, n/a. https://doi.org/10.1029/2011GC0039281

Tomkins, H. S., Powell, R., & Ellis, D. J. (2007). The pressure dependence of the zirconium-in-rutile thermometer. *Journal of Metamorphic Geology*, *25*(6), 703–713. https://doi.org/10.1111/j.1525-1314.2007.00724.x

Vanderhaeghe, O., Laurent, O., Gardien, V., Moyen, J.-F., Gébelin, A., Chelle-Michou, C., Couzinié, S., Villaros, A., & Bellanger, M. (2020). Flow of partially molten crust controlling construction, growth and collapse of the Variscan orogenic belt: The geologic record of the French Massif Central. *Bulletin de la Société Géologique de France*, *191*(25), 25. https://doi.org/10.1051/bsgf/2020013

Vavra, G. (1990). On the kinematics of zircon growth and its petrogenetic significance: A cathodoluminescence study. *Contributions to Mineralogy and Petrology*, *106*(1), 90–99. https://doi.org/10.1007/BF00306410

Vavra, G., Gebauer, D., Schmid, R., & Compston, W. (1996). Multiple zircon growth and recrystallization during polyphase Late Carboniferous to Triassic metamorphism in granulites of the Ivrea Zone (Southern Alps): An ion microprobe (SHRIMP) study. *Contributions to Mineralogy and Petrology*, *122*(4), 337–358. https://doi.org/10.1007/s004100050132

Vermeesch, P. (2018). IsoplotR: A free and open toolbox for geochronology. *Geoscience Frontiers*, *9*(5), 1479–1493. https://doi.org/10.1016/j.gsf.2018.04.001

von Raumer, J. F., & Stampfli, G. M. (2008). The birth of the Rheic Ocean—Early Palaeozoic subsidence patterns and subsequent tectonic plate scenarios. *Tectonophysics*, *461*(1), 9–20. https://doi.org/10.1016/j.tecto.2008.04.012

Wang, L., Kusky, T. M., Polat, A., Wang, S., Jiang, X., Zong, K., Wang, J., Deng, H., & Fu, J. (2014). Partial melting of deeply subducted eclogite from the Sulu orogen in China. *Nature Communications*, *5*, 5604. https://doi.org/10.1038/ncomms6604

Wiedenbeck, M., Alle, P., Corfu, F., Griffin, W. L., Meier, M., Oberli, F., & Spiegel, W. (1995). Three natural zircon standards for U-Th-Pb, Lu-Hf, trace element and REE analyses. *Geostandards Newsletter*, *19*, 1–23. https://doi.org/10.1111/j.1751-908X.1995.tb00147.x

Wiedenbeck, M., Hanchar, J. M., Peck, W. H., Sylvester, P., Valley, J., Whitehouse, M., Kronz, A., Morishita, Y., Nasdala, L., Fiebig, J., Franchi, I., Girard, J.-P., Greenwood, R. C., Hinton, R., Kita, N., Mason, P. R. D., Norman, M., Ogasawara, M., Piccoli, P. M., ... Zheng, Y. F. (2004). Further characterisation of the 91500 zircon crystal. *Geostandards and Geoanalytical Research*, *28*(1), 9–39. https://doi.org/10.1111/j.1751-908X.2004.tb01041.x

Yakymchuk, C., Clark, C., & White, R. W. (2019). 2. Phase relations, reaction sequences and petrochronology. In *Petrochronology: Methods and applications* (pp. 13–54). De Gruyter. https://doi.org/10.1515/9783110561890-003

Zack, T., Stockli, D. F., Luvizotto, G. L., Barth, M. G., Belousova, E., Wolfe, M. R., & Hinton, R. W. (2011). In situ U–Pb rutile dating by LA-ICP-MS: ^{208}Pb correction and prospects for geological applications. *Contributions to Mineralogy and Petrology*, *162*(3), 515–530. https://doi.org/10.1007/s00410-011-0609-4

Závada, P., Schulmann, K., Racek, M., Hasalová, P., Jeřábek, P., Weinberg, R. F., Štípská, P., & Roberts, A. (2018). Role of strain localization and melt flow on exhumation of deeply subducted continental crust. *Lithosphere*, *10*(2), 217–238. https://doi.org/10.1130/L666.1

SUPPORTING INFORMATION

Additional supporting information can be found online in the Supporting Information section at the end of this article.

Data S1. SuppInfo1.pdf – See details below.

Table S1. Operating conditions for the LA-ICP-MS equipment during zircon analyses.

Table S2. Operating conditions for the LA-ICP-MS equipment during apatite analyses.

Table S3. Operating conditions for the LA-ICP-MS equipment during rutile analyses.

Figure S1. X-Ray maps of a large polyinclusion in garnet.

Figure S2. Examples of plagioclase with low dihedral angle in amphibole–plagioclase and kyanite-rutile-plagioclase polyinclusions in garnet.

Figure S3. Th/Yb vs Nb/Yb plot after Pearce (2008) and Pearce (2014).

Figure S4. Representative Raman spectra of micro inclusions in zircon.

15251314, 0, Downloaded from https://onlinelibrary.wiley.com/doi/10.1111/jmg.12733 by Cochrane France, Wiley Online Library on [03/06/2023]. See the Terms and Conditions (https://onlinelibrary.wiley.com/terms-and-conditions) on Wiley Online Library for rules of use; OA articles are governed by the applicable Creative Commons License

Figure S5. Representative CL images of zircon in the diatexite embedding the studied eclogites.
Figure S6. Terra-Wasserburg and KDE plots of the U–Pb data in the zircon from the diatexite.
Figure S7. Representative CL images of apatites in the diatexite.
Figure S8. Terra-Wasserburg plot of the U–Pb data in the apatites from the diatexite.
Figure S9. *P–T* pseudosection constructed to study partial melting of amphiboles.
Figure S10. Summary of the radiometric data in the eclogites and calc-alkaline magmatism in the Morvan area.
Figure S11. Summary of the *P–T* paths and radiometric data in the Allochthonous units of the Variscan belt.
Figure S12: Summary of *P–T* paths and ages of the main metamorphic events in the French Massif Central and the Bohemian Massif. *P–T* paths for the FMC after the compilation of Benmammar et al. (2020) actualized with the data from Pitra et al. (2022). References for the ages in the FMC are this study, Lotout et al. (2018, 2020), Faure et al. (2014). See Figure S10 for details. *P–T* paths and ages for the Bohemian Massif after the compilation in Maierová et al. (2021). Note that the peak-temperature conditions in the FMC usually coincide with the peak-pressure conditions, but post-date a significant decompression from UHP conditions in the BM.
Data S2. SuppInfo2_BulkRocks.xlsx – Bulk rock compositions of the studied samples.
Data S3. SuppInfo3_U–Pb_Eclogites.xlsx – Summary of the operating conditions; U–Pb and trace element data for the standard and eclogites samples.
Data S4. SuppInfo4_U–Pb_Diatexite.xlsx – Summary of the operating conditions; U–Pb data for the standard and diatexite sample.

How to cite this article: de Hoÿm de Marien, L., Pitra, P., Poujol, M., Cogné, N., Cagnard, F., & Le Bayon, B. (2023). Complex geochronological record of an emblematic Variscan eclogite (Haut-Allier, French Massif Central). *Journal of Metamorphic Geology*, 1–29. https://doi.org/10.1111/jmg.12733

15251314, 0, Downloaded from https://onlinelibrary.wiley.com/doi/10.1111/jmg.12733 by Cochrane France, Wiley Online Library on [03/06/2023]. See the Terms and Conditions (https://onlinelibrary.wiley.com/terms-and-conditions) on Wiley Online Library for rules of use; OA articles are governed by the applicable Creative Commons License